

## Research Paper

# Multiscale insights into tunneling-induced ground responses in coarse-grained soils

Yipeng Xie<sup>a</sup>, Tongming Qu<sup>b,\*</sup>, Junsheng Yang<sup>c</sup>, Shuying Wang<sup>d</sup>, Jidong Zhao<sup>b</sup>

<sup>a</sup> College of Engineering, Ocean University of China, Qingdao 266404, China

<sup>b</sup> Department of Civil and Environmental Engineering, Hong Kong University of Science and Technology, Clearwater Bay, Kowloon, Hong Kong

<sup>c</sup> School of Civil Engineering, Central South University, Changsha 410075, China

<sup>d</sup> College of Civil and Transportation Engineering, Shenzhen University, Shenzhen 518060, China

## ARTICLE INFO

## Keywords:

Tunneling  
Coarse-grained soils  
Multiscale modeling  
Finite-element method (FEM)  
Discrete-element method (DEM)  
Soil arching

## ABSTRACT

This study presents a hierarchical multiscale approach that combines the finite-element method (FEM) and the discrete-element method (DEM) to investigate tunneling-induced ground responses in coarse-grained soils. The approach considers both particle-scale physical characteristics and engineering-scale boundary value problems (BVPs) simultaneously, accurately reproducing typical tunneling-induced mechanical responses in coarse-grained soils, including soil arching and ground movement characteristics observed in laboratory tests and engineering practice. The study also unveils particle-scale mechanisms responsible for the evolution of soil arching through the underlying DEM-based RVEs. The results show that the rearrangement of microstructures and the deflection of strong contact force chains drive the rotation of macroscopic principal stress and the formation of soil arch. The microscopic fabric anisotropy direction can serve as a quantitative indicator for characterizing soil arching zones. Moreover, the effects of particle size distributions (PSD) and soil densities on ground deformation patterns are interpreted based on the stress-strain responses and contact network characteristics of DEM RVEs. These multiscale insights enrich the knowledge of tunneling-induced ground responses and the same approach can be applied to other geotechnical engineering analyses in coarse-grained soils.

## 1. Introduction

Coarse-grained soils represent a typical cohesionless granular material commonly found in quaternary strata, such as glacial deposits, alluvium, and colluvium, and are frequently encountered in geotechnical engineering. With the rapid growth of transportation infrastructure and urban underground spaces, coarse-grained soils have become increasingly prevalent as a ground condition for tunneling. However, the lack of interparticle cohesion makes this type of soil highly sensitive to disturbances induced by underground construction, as demonstrated by numerous engineering practices over the past decades (Lin et al., 2021; 2022a; Chen et al., 2023a,b; Guo et al., 2023). Face stability (Chen et al., 2015), surface settlement (Fargnoli et al., 2013; Franza et al., 2019), ground collapse (Hu et al., 2021; Shao et al., 2022), and deformation of the existing surface or buried structures (Boldini et al., 2021; Lin et al., 2022a; Bao et al., 2024) are all concerns when tunneling in coarse-grained soils. Moreover, the microstructures of coarse-grained soils exhibit considerable variation due to the complex deposition

process and stress history, resulting in high variability in tunneling-induced ground responses (Mair and Taylor, 1997; Franza et al., 2019; Shen et al., 2022). Therefore, accurate understanding and prediction of tunneling-induced ground responses in coarse-grained soils is a key ingredient in informing geotechnical design and risk assessment.

Tunneling-induced responses in coarse-grained soils have been investigated through field investigations, physical modeling tests, and numerical studies. The trapdoor tests developed by Terzaghi (1936) have been a popular example of reproducing the soil arching phenomenon caused by underground disturbances. In recent decades, numerous laboratory tests have investigated the ground movement, load transfer, and stress redistribution triggered by soil arching (Terzaghi, 1936; Vardoulakis et al., 1981; Dewoolkar et al., 2007), and some mathematical models for soil arching evolution have been developed based on limit equilibrium method (Terzaghi, 1943; Evans, 1983; Iglesia et al., 1999; Lin et al., 2022b). Recent trapdoor tests have focused on understanding how complex loading conditions (e.g., cyclic or asymmetrical loading) (Zhao et al., 2021; Chen et al., 2023a,b) or microstructures of

\* Corresponding author.

E-mail address: [tongmingqu@ust.hk](mailto:tongmingqu@ust.hk) (T. Qu).

<https://doi.org/10.1016/j.compgeo.2025.107319>

Received 5 September 2024; Received in revised form 4 April 2025; Accepted 1 May 2025

0266-352X/© 2025 Elsevier Ltd. All rights are reserved, including those for text and data mining, AI training, and similar technologies.

the granular soils (e.g., soil density or particle shape) (Ali et al., 2020; Liu et al., 2022) affect the soil arching behavior. To replicate the stress field of tunneling prototypes and full-scale conditions, advanced physical tunnel modeling techniques have been developed. These techniques involve the utilization of various devices such as the pressurized airbag device (Atkinson et al., 1975; Hagiwara et al., 1999), fluid-filled flexible membrane model (Loganathan et al., 2000; Marshall et al., 2012), and rigid boundary mechanical model (Lee, 2009; Song and Marshall, 2020) to simulate 2D plane-strain tunnel volume loss in centrifugal tests. Furthermore, some 3D large-scale tests have incorporated miniature shield machines (Nomoto et al., 1999; Hu et al., 2020; Lin et al., 2022a) to reproduce the shield construction process. With these techniques, the ground movement and tunnel stability of the greenfield tunneling have been investigated, as well as the soil interactions with pipelines, pile foundations, and surface structures induced by tunneling.

Considering the cost and operability limitations of physical tests, numerical approaches have been widely applied for the analysis of tunneling-related geotechnical problems in coarse-grained soils. For instance, the finite element method (FEM) with constitutive soil models is often used for comparison analysis with analytical solutions, physical tests, and field monitoring (Migliazza et al., 2009; Fargnoli et al., 2015). Once the numerical models are calibrated, they can provide more detailed information than physical tests to illustrate the ground stress distribution and failure pattern. Notably, a FEM model incorporating randomly distributed rigid block elements has been used to simulate the heterogeneous structures of the widely graded coarse-grained soils and revealed the non-uniform distribution of the soil stress and displacement fields (Du et al., 2019; Xie et al., 2019; Napoli et al., 2021; Wang et al., 2023). In addition to the aforementioned continuum-based numerical methods, the discrete element method (DEM) can explore more on the particle-scale mechanical behaviors, such as the effect of the soil microstructures on the tunneling-induced ground response (Yin et al., 2020; Xie et al., 2023), and the force-chain network evolution activated by tunneling (Wang et al., 2019; Hu et al., 2021), and the coupling behaviors between soil movement, discharging and tunnel cutterhead (Qu et al., 2019; Hu et al., 2020; Shao et al., 2022). Despite their successes, there remains an apparent gap between these numerical methods and engineering practice.

The core of continuum-based numerical methods is the assumed constitutive soil models, which are often criticized as phenomenological and rely on complex parameter calibration and model validation processes (Qu et al., 2021a,b; Wang et al., 2023a,b). For coarse-grained soils in tunneling scenarios, determining suitable constitutive models is even more challenging due to soil microstructure heterogeneity, as well as the high mechanical dependence on diverse sedimentary states and complicated loading paths (Mair and Taylor, 1997; Guo and Zhao, 2014 and 2015). DEM schemes bypass the phenomenological hypotheses but are computationally expensive, especially for wide particle gradation systems (Berger and Hrenya, 2014; Wang et al., 2024). Therefore, coarse-graining or scale-down modeling (similar to centrifugal tests, where only the model box is reduced while maintaining the prototypical size of soil grains) is commonly used to improve the computational efficiency in most tunneling-related DEM studies. However, these approaches inherently increase the size ratio between soil grains and tunnel, introducing non-negligible geometric similarity errors into the simulated ground mechanical behaviors, such as tunnel face stability and shear band development (Stone and Wood, 1992; Garnier et al., 2007). Due to the above-mentioned reasons, conventional numerical schemes still struggle to produce accurate predictions on tunneling-induced mechanical responses of coarse-grained soils on the engineering scale, especially in assessing the effect of various microstructures on the macroscopic ground responses.

To overcome the limitations of pure continuum and discrete-based numerical schemes, multiscale modelling methods have been developed and applied in geotechnical analysis. One of the common multiscale approaches is the FEM-DEM concurrent multiscale modelling

method. This method constructs both discrete medium and deformable continuous medium in the same physical domain, where the discrete medium is used specifically for constructing localized regions that require additional attention (Cheng et al., 2023). This improves the computational efficiency compared with pure DEM methods. This method has been applied to tunneling problems in granular soils (Yin et al., 2020) and jointed rock mass (Fang et al., 2023). However, for an engineering-scale model, it is still expensive to completely reproduce the precise soil grain size or joint density within the local region around the tunnel. As a result, the current FEM-DEM concurrent multiscale tunneling model still relies on coarse-graining simplification. Alternatively, the recently developed hierarchical multiscale approach FEM  $\times$  DEM provides a different modelling strategy (Guo and Zhao, 2014 and 2015; Desrues et al., 2019). The coupling object of the hierarchical multiscale approach is also usually FEM and DEM. In contrast to the concurrent multiscale method, the FEM is used to simulate the physical domain of a boundary value problem (BVP), and each integration point of the mesh is embedded with a DEM-based representative volume element (RVE). The soil constitutive response is derived from the DEM solution of each RVE, which avoids conventional phenomenological hypotheses and can faithfully record the particle-scale fabric evolution history. The computational efficiency of FEM in solving large-scale BVPs is retained, and the hierarchical coupling structure can conveniently process DEM assemblies in parallel. This approach has been implemented in the analysis of BVPs involving the bearing capacity of anisotropic sand footing (Guo et al., 2022), seepage stability of gap-graded soil slope (Hu et al., 2022), and the borehole stability in high porosity rocks (Wu et al., 2018), demonstrating the capability of bridging microstructure with macroscopic behaviors. Inspired by this approach, some researchers have developed the FE<sup>2</sup> (FEM  $\times$  FEM) multiscale model to explore the tunneling-induced rock's fracture damage in clay rocks (Mourlas et al., 2023). However, this model cannot reveal the ground response of granular soils in urban tunnel scenarios because its microscopic modelling is still continuum-based.

In this study, we apply the FEM  $\times$  DEM hierarchical multiscale approach to revisit tunneling-induced ground responses in coarse-grained soils. The methodology of the multiscale approach is briefly introduced, followed by the numerical modeling details of the tunneling BVP (including the ground initialization and the description of volume loss) and the RVE packings of coarse-grained soils. The effect of cover-to-diameter ratio ( $C/D$ ), particle size distribution (PSD) and soil density on the soil arching behavior and ground movement are investigated in detail. In particular, we correlate the evolution of RVE-scale fabric, the particle arrangement and force chain networks, and stress-strain responses with macroscopic results, providing a multiscale insight to identify the mechanism behind tunneling-induced soil arching evolution in coarse-grained soils.

## 2. Multiscale Approach

The hierarchical multiscale approach in this study uses two open-source codes, *YADE* (Kozicki and Donze, 2009) and *Esript* (Gross et al., 2007), to couple FEM and DEM. The coupling scheme is schematically illustrated in Fig. 1, where the three-dimensional tunneling problem is simplified as a two-dimensional plane-strain BVP. Tunneling-induced volume loss typically results from imbalanced soil discharging at the excavation face, the annular cavity at the shield tail, long-term lining deformation and soil consolidation (Vu et al., 2016). Here, volume loss is equivalently considered using a displacement boundary condition (Loganathan and Poulos, 1998). The physical domain of a BVP is first discretized as a FEM mesh, and a DEM assembly prepared with a suitable initial state is attached to each Gauss integration point of the FEM mesh, serving as the RVE. At each Gauss point, the FEM passes the deformation information (strain  $\epsilon$  plus rotation  $\omega$ ) to the corresponding RVE as the boundary condition. The local material responses, including stress and tangent operators, are derived from DEM simulation and

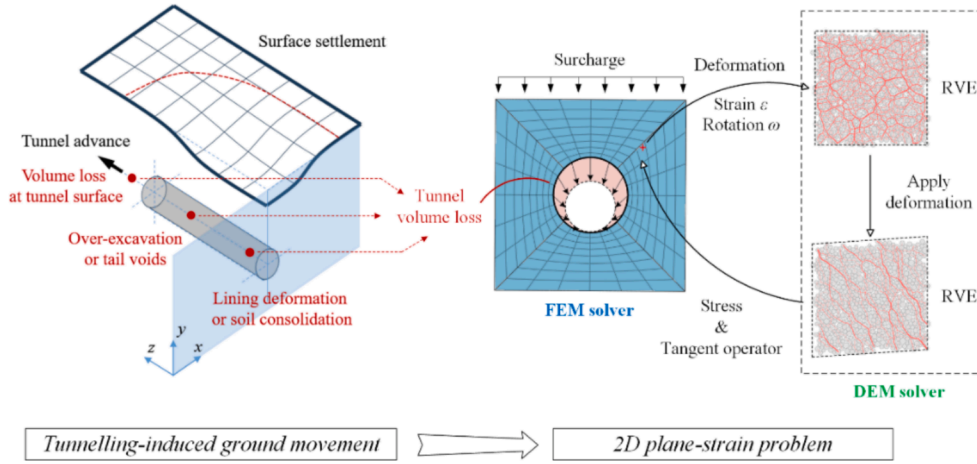


Fig. 1. Illustration of the modeling procedure of the multiscale approach.

updated to the FEM solver for the next loading step (Guo and Zhao, 2014 and 2015). The methodology and formulation are briefly introduced in this section.

The governing equilibrium equation for the quasi-static BVP considering the gravity is written as:

$$\sigma_{ij,j} + b_i = 0 \quad (1)$$

where  $\sigma_{ij}$  is the stress tensor, and  $b_i$  is the unit body force of gravity. After the FEM discretization, Eq. (1) can be rewritten as the following equation:

$$\mathbf{K}\mathbf{u} = \mathbf{f} \quad (2)$$

where  $\mathbf{K}$  is the stiffness matrix;  $\mathbf{u}$  is the nodal displacement to be resolved, and  $\mathbf{f}$  is the nodal force vector lumped from the applied boundary traction. Unlike the conventional FEM approach, any phenomenological assumptions used in constitutive models are abandoned and the material constitutive response is directly obtained by separate DEM simulations at each FEM Gauss point in the multiscale approach. Therefore, the primary solution procedure of the multiscale approach in a global loading step consists of the following steps:

- Use an initial  $\mathbf{K}$  to solve a trial FEM solution;
- Interpolate the displacement gradient  $u_{i,j}$  at each Gauss point and apply them as boundary conditions for corresponding RVE packings;
- Obtain the RVE's responses with the homogenized stress tensor  $\sigma_{ij}$  (see Eq. (3)) and tangent modulus tensor  $D_{ijkl}$  (see Eq. (4)) from the DEM solutions:

$$\sigma_{ij} = \frac{1}{V} \sum_{N^c} f_i^c d_j^c \quad (3)$$

$$D_{ijkl} = \frac{1}{V} \sum_{N^c} (k_n n_i^c d_j^c n_k^c d_l^c + k_t t_i^c d_j^c t_k^c d_l^c) \quad (4)$$

where  $V$  is the volume of RVE packing;  $N^c$  is the contact number;  $\mathbf{f}^c$  and  $\mathbf{d}^c$  are the contact force and contact branch vector, respectively;  $\mathbf{n}^c$  and  $\mathbf{t}^c$  are unit vectors along normal and tangent directions at a contact, respectively;  $k_n$  and  $k_t$  are interparticle normal contact stiffness and tangent contact stiffness, respectively; the subscripts i.e.  $i, j, k, l$  are indices in  $\{1, 2\}$  for 2D, and  $\{1, 2, 3\}$  for 3D, with 1, 2, 3 representing  $x, y, z$  directions in the global coordinate system.

- Assemble the stiffness matrix  $\mathbf{K}$  in Eq. (2) by using the updated global stress tensor  $\sigma$  and tangent operator  $\mathbf{D}$  as follows:

$$\mathbf{K} = \int_{\Omega} \mathbf{B}^T \mathbf{D} \mathbf{B} d\Omega \quad (5)$$

where  $\Omega$  is the problem domain;  $\mathbf{B}$  is the strain–displacement matrix.

- Evaluate the residual force  $R$  with a target tolerance by

$$\mathbf{R} = \int_{\Omega} \mathbf{B}^T \sigma d\Omega - \mathbf{f} \quad (6)$$

and then perform Newton–Raphson iteration over (b) to (e) to find a converged solution of Eq. (2).

Based on the homogenized stress tensor in Eq. (3), the mean effective stress  $p$ , and the deviatoric stress  $q$ , can be obtained (for 2D) from

$$p = -\frac{1}{2} \sigma_{ii} \quad (7)$$

$$q = \sqrt{\frac{1}{2} s_{ij} s_{ij}} \quad (8)$$

where  $s_{ij}$  is the deviatoric stress tensor, and  $s_{ij} = \sigma_{ij} - p \delta_{ij}$ , with  $\delta_{ij}$  being the Kronecker delta. Meanwhile, the strain tensor is derived from the displacement gradient tensor  $u_{i,j}$

$$\varepsilon_{ij} = (u_{ij} + u_{ji})/2 \quad (9)$$

The volumetric strain  $\varepsilon_v$  and the deviatoric strain  $\varepsilon_q$  can be expressed as follows:

$$\varepsilon_v = -\varepsilon_{ii} \quad (10)$$

$$\varepsilon_q = \sqrt{2e_{ij}e_{ij}} \quad (11)$$

where  $e_{ij}$  is the deviatoric strain tensor, and  $e_{ij} = \varepsilon_{ij} - \frac{1}{2} \varepsilon_v \delta_{ij}$ .

### 3. Model Setup

#### 3.1. RVE of Coarse-grained Soils

One objective of this study is to examine the effect of the microstructure of coarse-grained soils on the macroscopic ground responses induced by tunneling. To achieve this, we designed DEM assemblies including two different PSDs, i.e., CPS and CPG, and two packing densities as RVEs in multiscale analysis, respectively. The DEM assembly is enclosed by periodic boundaries (Qu et al., 2021a,b), and the model in YADE code is modified for 2D analysis by generating all sphere elements in the same  $xy$  plane and restraining all degrees of freedom in the  $z$ -direction. This is an approximation of the plane strain problem (Kozicki and Donze, 2009). The designed PSDs are categorized into two different coarse-grained soils as ASTM D2487-17, i.e., poorly graded sand (CPS) and well-graded gravel (CPG), and the PSD curves are shown in Fig. 2. The designed PSDs show similarity with some typical sands and gravels in gradation parameters  $C_u$  and  $C_c$ . To ensure that the mechanical

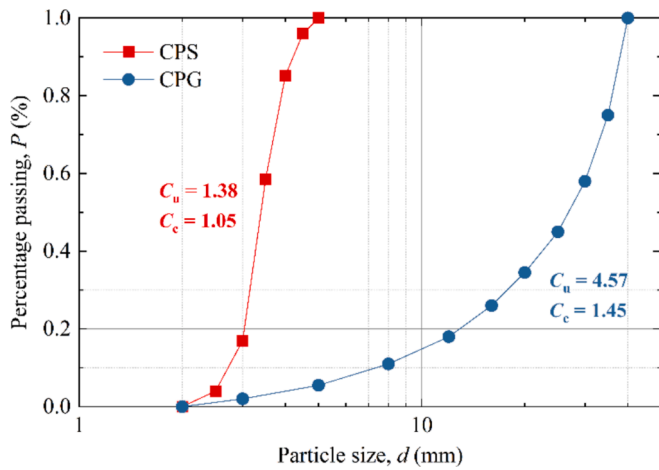


Fig. 2. PSD curves for DEM RVEs in multiscale modeling.

response of RVE is statistically representative, the size of the RVE (particle number) was determined using a combined numerical-statistical approach (Stroeven et al., 2004). The detailed documentation of the determination process can be found in Appendix A. To strike a balance between RVE's representativeness and computational efficiency, we set the RVE size as 700 particles for CPS and 1500 particles for CPG, where the CPG is of higher structural heterogeneity.

Sphere-shaped uncrushable particles with a linear force–displacement contact law, tangentially capped by Coulomb's friction criterion, were employed to simulate the behavior of soil grains and their inter-particle contact interactions. In addition, the rolling resistance model was introduced to reproduce the anti-rotation effect caused by the real particle shape (Iwashita and Oda, 1998; Qu et al., 2022; Song et al., 2024). The coarse-grained soil particles were classified by size into three types of grains: coarse sand ( $d = 2$  to  $4.75$  mm), fine gravel ( $d = 4.75$  to  $19$  mm), and coarse gravel ( $d = 19$  to  $40$  mm), following ASTM D2487-17 guidelines. The calibration of the microscopic parameters started with the category of coarse sand, which completely constituted the CPS soils shown in Fig. 2. The microscopic parameters were adjusted to match the shear strength and dilatancy of the CPS specimens to typical coarse sands. Based on the parameters of the coarse sand category, the fine gravel and coarse gravel were sequentially set with higher inter-particle friction angles and rolling resistance coefficients, to match the previous laboratory observation that the shear resistance of coarse-grained soils grows with an increasing particle size (Nurul Islam et al., 2011; Alhani et al., 2020; Wang et al., 2022). All of the calibrated microscopic parameters are shown in Table 1.

The discrete element model was first consolidated to an initial state with isotropic stress, and then stored as an RVE for the stress–strain behavior examination and the following multiscale modeling. During initial consolidation, a temporary friction coefficient  $\mu_t = 0.0$  was set for generating the dense RVE, and the relatively loose RVE was prepared with  $\mu_t = 0.45$  (Gong et al., 2024). The RVE packings (visualized by particle arrangement and contact forces network) of CPS\_D, CPS\_MD, and CPG\_D are plotted in Fig. 3. Drained biaxial testing was conducted on these DEM RVEs to examine their shear strength and dilatancy. The biaxial tests were performed under confined pressures of 100 kPa, 200

kPa, and 400 kPa, respectively, with a strain rate of 0.01. The inertial number for each RVE was found to be less than  $1 \times 10^{-4}$ , indicating a quasi-static simulation (Nguyen et al., 2017).

The stress–strain curves, along with their peak failure line and critical state line in the  $p$ - $q$  plane, are presented in Fig. 4. The  $\phi_p$  and  $\phi_{cs}$  values of each RVE can be estimated from these lines, and the  $\psi_{max}$  can be estimated from the maximum slope of the volumetric strain curves. The mechanical parameters obtained are summarized in Table 2. As typical granular soils, the numerical specimens exhibited greater deviatoric stresses with increasing confining pressure, along with more noticeable contraction. For CPS\_MD, the clear peak in deviatoric stress with dilation becomes less pronounced. The CPS specimens demonstrate properties that reasonably agree with the dense and loose Hostun sands (Schanz and Vermeer, 1996). Additionally, CPG displays higher  $\phi_p$  and  $\psi_{max}$  values compared to CPS, consistent with previous research indicating that granular soils with wider gradations tend to have higher peak shear strengths and greater dilatancy, while their critical shear strengths remain relatively unaffected (Ahmed et al., 2023). Despite being a simplified representation of real soil, the biaxial tests conducted on the 2D spherical-shape DEM RVEs showed that the DEM-based materials exhibited the typical mechanical behavior of coarse-grained soils. This finding lays a solid foundation for the reliability of the multiscale tunneling model.

### 3.2. Simulation of Tunneling-induced Ground Responses

In this study, the tunneling process is simplified as a 2D plane strain BVP, and the multiscale modeling scheme is illustrated in Fig. 5. The prototype of the multiscale numerical model is a tunnel with a diameter of 5.0 m, and the cover-to-diameter ratio  $C/D$  is set as 2.0, 3.0 and 4.0, respectively. To improve the computational efficiency of the multiscale analysis, only half of the physical domain is modeled ( $35 \text{ m} \times 35 \text{ m}$ , as shown in Fig. 5(a)). The rationale for this simplification is based on the symmetry of boundary conditions and is substantiated by previous observations from engineering fields and physical modelling tests (Lee et al., 2004; Franza et al., 2019; Burke et al., 2020). However, it is noteworthy that even in nearly isotropic granular media, fabric evolution and non-coaxial responses can induce anisotropy and trigger strain localization, thereby disrupting perfect symmetry (Guo and Zhao, 2014). The simplified half-domain model adopted in this study cannot capture this characteristic.

The BVP domain is discretized by a FEM mesh composed of eight-node quadrilateral elements (821 elements for  $C/D = 2.0$ , 836 elements for  $C/D = 3.0$ , and 892 elements for  $C/D = 4.0$ ). Each element has four integration points (induced integration). A finer mesh is generated close to the tunnel boundary. The initial RVEs are consolidated by an isotropic stress of 1.0 kPa and embedded at the integration points (as shown in Fig. 5(b)). Considering the subsequent gravity consolidation process of the BVP's physical domain, greater initial consolidation stresses may result in an over-consolidated state of RVEs near the ground surface. The 2D void ratios of the initial RVE are 0.116 (CPG\_D), 0.184 (CPS\_D), and 0.252 (CPS\_MD), respectively. Note that the RVEs located near the ground surface typically experience low-stress levels, which might lead to numerical instability in the FEM simulation. To mitigate this issue, a small surcharge load of 1.0 kPa is applied to the top surface. The soil unit weights are set as  $2200 \text{ kN/m}^3$  (CPG\_D),  $2000 \text{ kN/m}^3$

Table 1  
Parameters for the DEM-based RVEs.

Particle class	Size range (mm)	Contact Young's modulus (GPa)	Contact stiffness ratio ( $k_t/k_n$ )	Damping ratio	Interparticle friction angle ( $^\circ$ )	Rolling resistance coefficient
Coarse gravel	[40, 19]	5.0	0.8	0.3	50	0.8
Fine gravel	[19, 4.75]	4.0	0.7		40	0.7
Coarse sand	[4.75, 2]	3.0	0.5		25	0.6

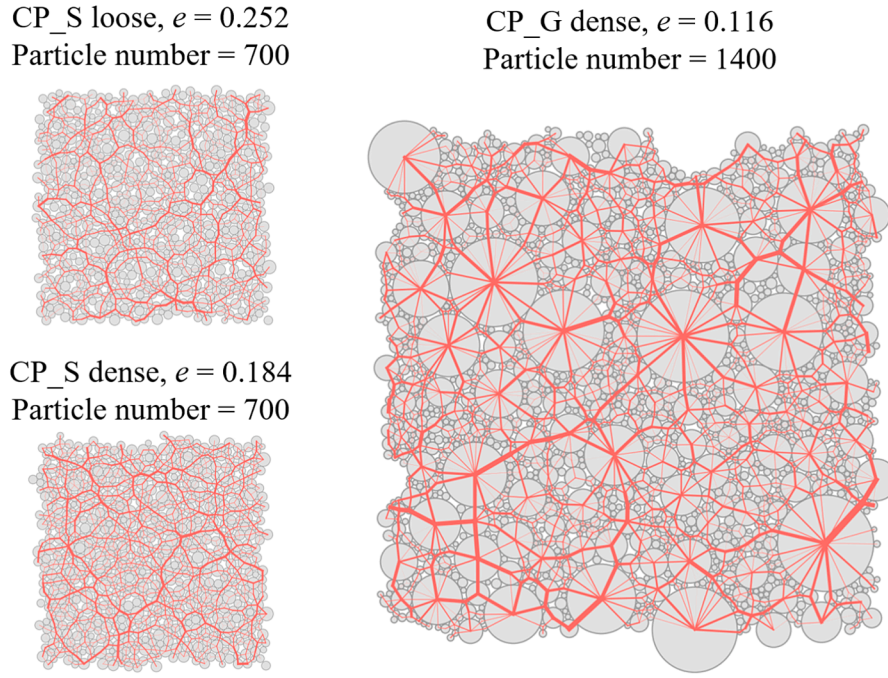


**Fig. 3.** RVE packings after isotropic consolidation (the red lines represent the contact forces, and the width of these lines is related to the relative magnitude of contact forces).

(CPS\_D), and 1800 kN/m<sup>3</sup> (CPS\_MD), respectively, following BS 8002–2015 guidelines.

In the multiscale analysis of tunneling, the first step involved solving the BVP to achieve a natural equilibrium state under the influence of gravity. Unlike using an identical DEM RVE and uniformly distributed stress field throughout the multiscale model (Guo and Zhao, 2015; Mourlas et al., 2023), this gravity consolidation stage allows RVEs located at various locations to reach a naturally consolidated state of stress and fabric, thereby replicating the stress gradient variation in the natural ground conditions. During the gravity equilibrium phase, the stress condition was applied to the semi-circular boundary to satisfy the equilibrium requirements (see Fig. 5 (c)):

$$\sigma_{\text{tunnel}}^n = l^2 \sigma_{xx} + m^2 \sigma_{yy} + 2lm\tau_{xy} \quad (15)$$

$$\sigma_{\text{tunnel}}^r = lm(\sigma_{yy} - \sigma_{xx}) + (l^2 - m^2)\tau_{xy} \quad (16)$$

where  $\sigma_{\text{tunnel}}^n$  and  $\sigma_{\text{tunnel}}^r$  are normal and shear stresses applied to an arbitrary integration point on the tunnel boundary. The symbols  $l$  and  $m$  are direction cosines between the normal direction out of the tunnel boundary and the positive direction of the  $x$  or  $y$  axes, respectively, where  $l = \cos(N, x)$  and  $m = \cos(N, y)$ .  $\sigma_{yy}$  and  $\sigma_{xx}$  denote vertical and horizontal stresses, respectively, where  $\sigma_{yy} = -\gamma(H-y_i)$ , and  $\sigma_{xx} = K_0\sigma_{yy}$ . During the natural consolidation process,  $\sigma_{yy}$  and  $\sigma_{xx}$  are equal to the major and minor principal stress, respectively, therefore the shear stress  $\tau_{xy}$  is considered to be zero. Notably, the coefficient of earth pressure  $K_0$  lacks an accurate theoretical solution because it is influenced by stress paths and granular fabric. Therefore, before the gravity equilibrium of the tunnel model, the  $K_0$  value was calibrated from a parallel rectangular model without a tunnel boundary and contained the same DEM RVEs. In the case of CPS\_D,  $C/D = 3.0$ , the stress field after gravity equilibrium is shown in Fig. 6(a). The stress distributions of  $\sigma_{yy}$  and  $\sigma_{xx}$  show linear gradients with depth along the vertical direction, while remaining highly uniform along the horizontal direction. Although the  $\tau_{xy}$  results indicate a slight stress deflection near the tunnel boundary, the magnitude of the  $\tau_{xy}$  suggests that this deflection is estimated to be no greater than 0.5 degrees. Fig. 6(b) presents the stress distribution along the

vertical measurement path near the tunnel boundary. The correlation of  $\sigma_{yy}$  with the overburden depth agreed well with the theoretical solution of earth pressure. The measured  $K_0$  values are similar to some observations in the naturally consolidated ground (Chevalier et al., 2012; Garcia and Bray, 2019), and the nonlinear correlation between  $K_0$  and  $\sigma_{yy}$  is in agreement with laboratory findings (Chu and Gan, 2004; Gu et al., 2018). Additionally, a comparison of the RVE's fabric before and after the equilibrium process is shown in Fig. 6(c). The interparticle contact forces evolve from an isotropic agreement to a predominantly vertical alignment under the impact of gravity consolidation.

During the loading stage, the tunnel volume loss  $V_{It}$  that increases with pseudo time  $T$  (loading steps) is used to trigger ground movement and progressive failure. Fig. 5(d) illustrates the modeling of tunnel volume loss using an eccentric displacement boundary (maximum displacements at the tunnel crown and zero displacements at the invert). This boundary represents a commonly recognized pattern of ground movement surrounding shallow tunnels, often caused by factors such as over-excavation, inadequate void filling, and deflection of the tunnel lining (Loganathan and Poulos, 1998). In multiscale modeling, the displacement  $u_i$  of an arbitrary node on the tunnel boundary is as follows:

$$u_i^x = \Delta u \sin\theta \quad (17)$$

$$u_i^y = \Delta u \cos\theta \quad (18)$$

$$\Delta u = D \left( 1 - \sqrt{1 - \Delta V_{It}} \right) \quad (19)$$

where  $\theta$  and  $\Delta u$  are illustrated in Fig. 5. In the multiscale analysis, a  $V_{It}$  of 20 % was implemented in 80 loading steps. Notably, the simulated  $V_{It}$  is higher than the monitored values in the tunnel construction field (usually in the range of 1 % to 5 %) for a clear observation of the ground progress destabilization. This  $V_{It}$  setup was usually adopted by previous physical modeling tests (Lee et al., 2004; Lee, 2009; Boonsiri and Takemura, 2015).

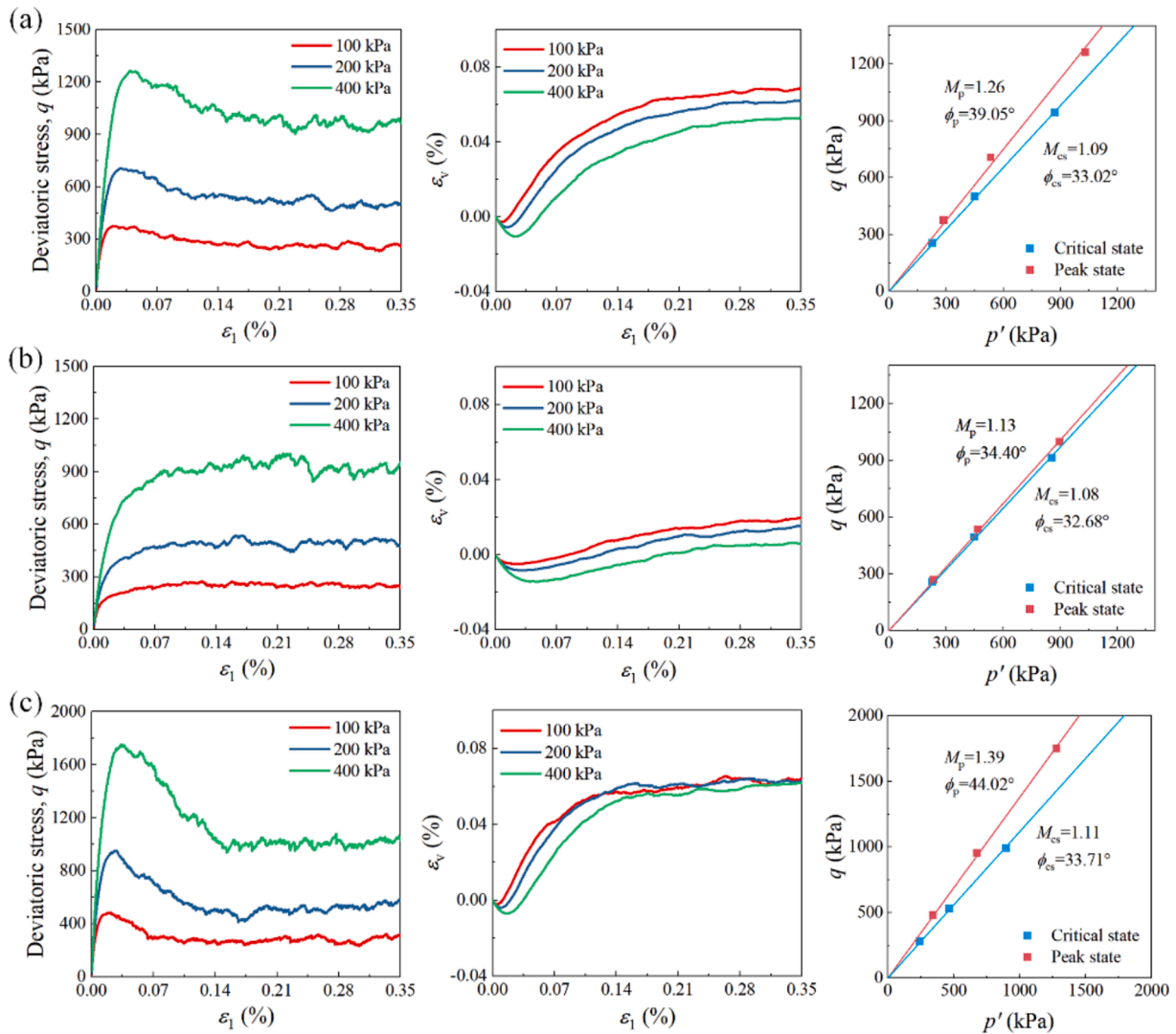


Fig. 4. Biaxial stress–strain curves, peak failure lines and critical state lines for DEM RVEs of (a) CPS\_D, (b) CPS\_MD, and (c) CPS\_G.

**Table 2**  
Calibrated mechanical properties for simulated coarse-grained soils.

Material	$\phi_p$	$\phi_{cs}$	$\psi_{max}$
CPS_D	39.1°	33.0°	14.0°
CPS_MD	34.4°	32.7°	3.1°
CPG_D	44.0°	33.7°	17.3°
Hostun sand (dense) (Schanz and Vermeer, 1996)	41.9°	34.8°	13.3°
Hostun sand (loose)	34.4°	34.4°	0.0°
(Schanz and Vermeer, 1996)			
Leighton Buzzard sands (dense) (Lanzano et al., 2016)	39.4°	33.4°	12.3°

#### 4. Macroscopic Ground Responses Induced by Tunneling

##### 4.1. Soil Arching and Ground Movement

Previous studies have confirmed that the volume loss arising from the construction of underground structures can trigger the soil arching phenomenon (Iglesia et al., 2014; Zhao et al., 2021; Lin et al., 2022). This phenomenon is qualitatively illustrated in Fig. 7. When volume loss occurs, the ground moves towards the underground opening to compensate for the volume loss. The soil mass adjacent to the opening experiences large vertical displacement and volume dilation, commonly

referred to as the soil active region. Above the active region, the soil particles are compacted due to the horizontal movement of the ground, leading to a deflection in the principal stress paths and the formation of a soil arch within the ground. The stability of this soil arch relies on the shear resistance of the internal soils, and the support provided by the active soils below (Zhao et al., 2021). As the volume loss increases, the volume dilation of the active soils reaches the limit state, making it difficult for the soil arch to remain self-stabilized without additional support. Therefore, the soil arch will partially collapse, giving rise to new active soils. The ultimate collapse of the soil arch will result in the formation of two nearly vertical failure planes connected with the ground surface, causing the entire soil column above the underground structure to slide.

In engineering practice, both ground surface and subsurface settlements are frequently measured to assess and characterize ground movement. Settlement trough curves are developed to represent the distribution of ground settlement. In this study, the modified Gauss curve (Vorster et al., 2005) is employed for quantifying the settlement trough, with the curve being described as follows:

$$S_v(x) = S_{max} \frac{n}{(n-1) + \exp[\alpha(x/i)^2]} \quad (20)$$

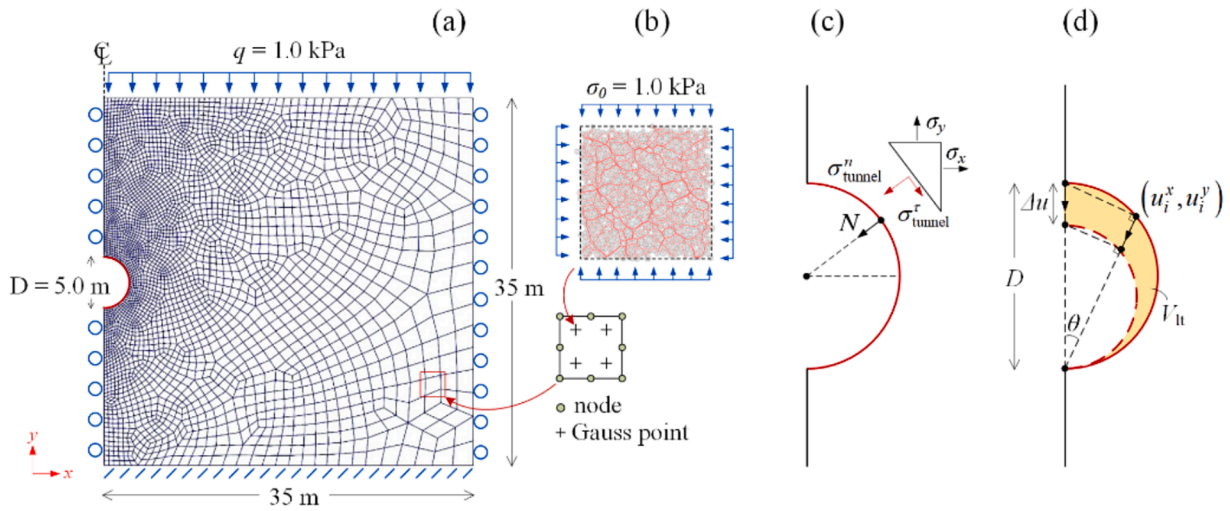


Fig. 5. Illustration of the multiscale modeling scheme, including (a) BVP and FEM mesh; (b) Embedded DEM-based RVE; (c) Stress-controlled boundary conditions in gravity equilibrium stage; (d) Displacement-controlled boundary conditions in loading stage.

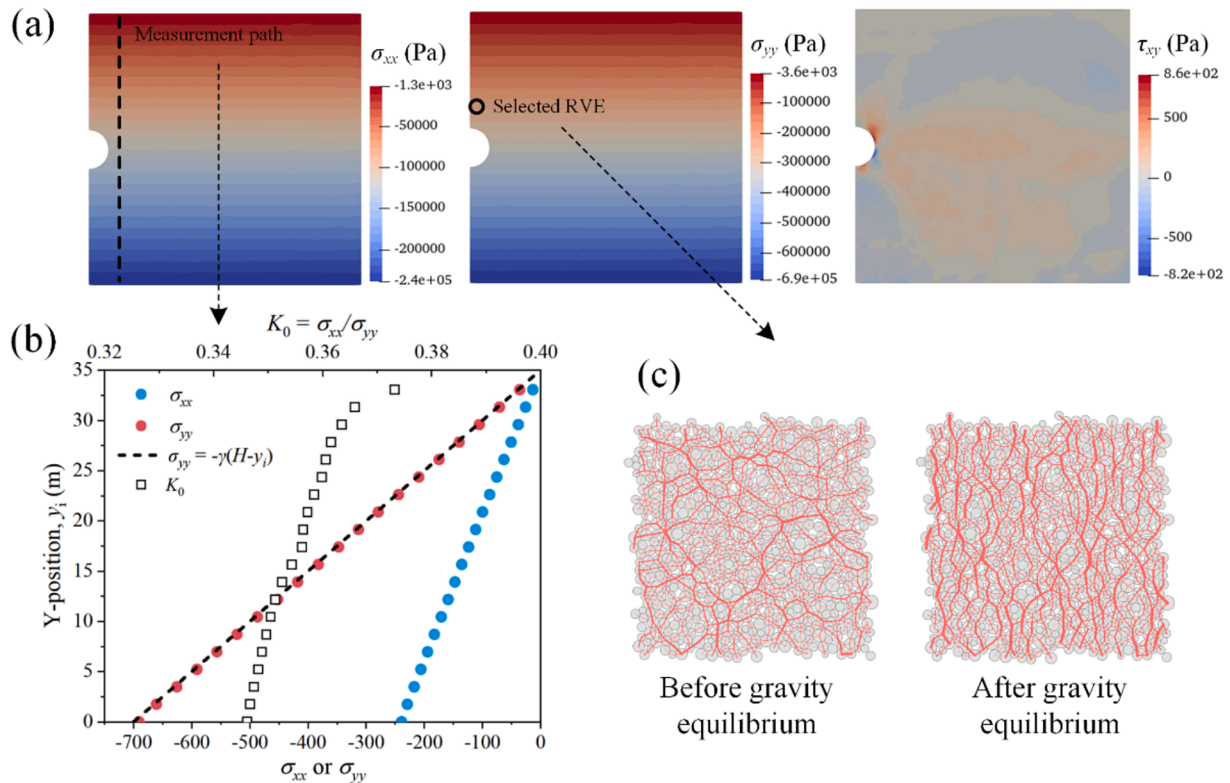


Fig. 6. Initial state after gravity equilibrium, including (a) Stress field; (b) Stress and  $K_0$  distribution along a vertical measurement path; (c) Comparison of the RVE's fabric before and after the equilibrium.

$$n = e^{\alpha \frac{2\alpha - 1}{2\alpha + 1}} + 1 \quad (21)$$

where ground settlement  $S_v$  is expressed as the function of horizontal distance  $x$  from any location to the tunnel centerline;  $S_{max}$  is the maximum vertical settlement;  $i$  represents the horizontal distance between the inflection point to the tunnel centerline;  $\alpha$  is a shape parameter. Compared with the standard Gaussian curve, the shape parameter  $\alpha$  provides a higher degree of freedom for more effective settlement trough fitting especially for shallow tunnels buried in granular soils (Vorster et al., 2005; Marshall et al., 2012).

According to the aforementioned multiscale modeling scheme, the ground movement with soil arching behavior is accurately reproduced in CPS\_D soils in this section. Fig. 8 shows the evolution of ground displacement with increasing  $V_{lt}$  for different  $C/D$  ratios. The maximum value of the color map at each  $V_{lt}$  stage represents the maximum vertical displacement of the tunnel crown, highlighting the impact of the soil arch on displacement transfer. Upon activation by tunnel volume loss, a distinct parabolic-shaped region of active soils with significant displacement appears near the tunnel crown. With an increase in  $V_{lt}$ , the ground displacement away from the tunnel crown becomes more concentrated toward the model's centerline in the horizontal direction,

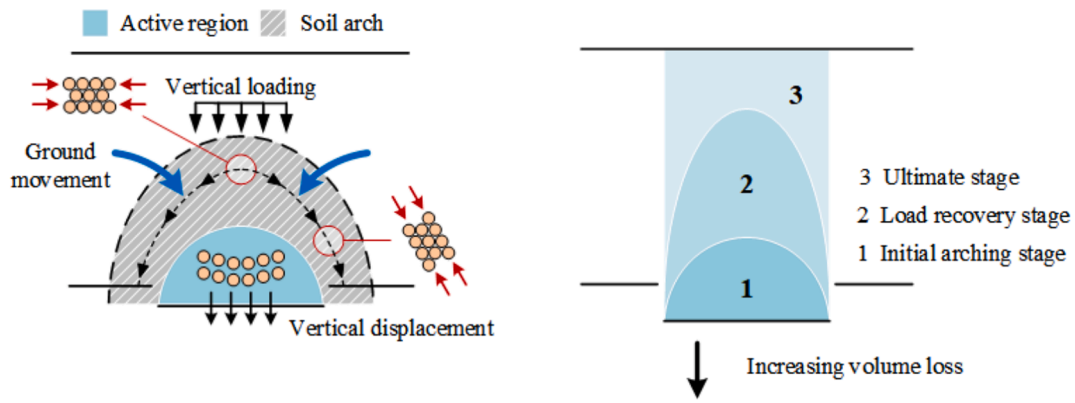


Fig. 7. Schematic diagram of the soil arching behavior.

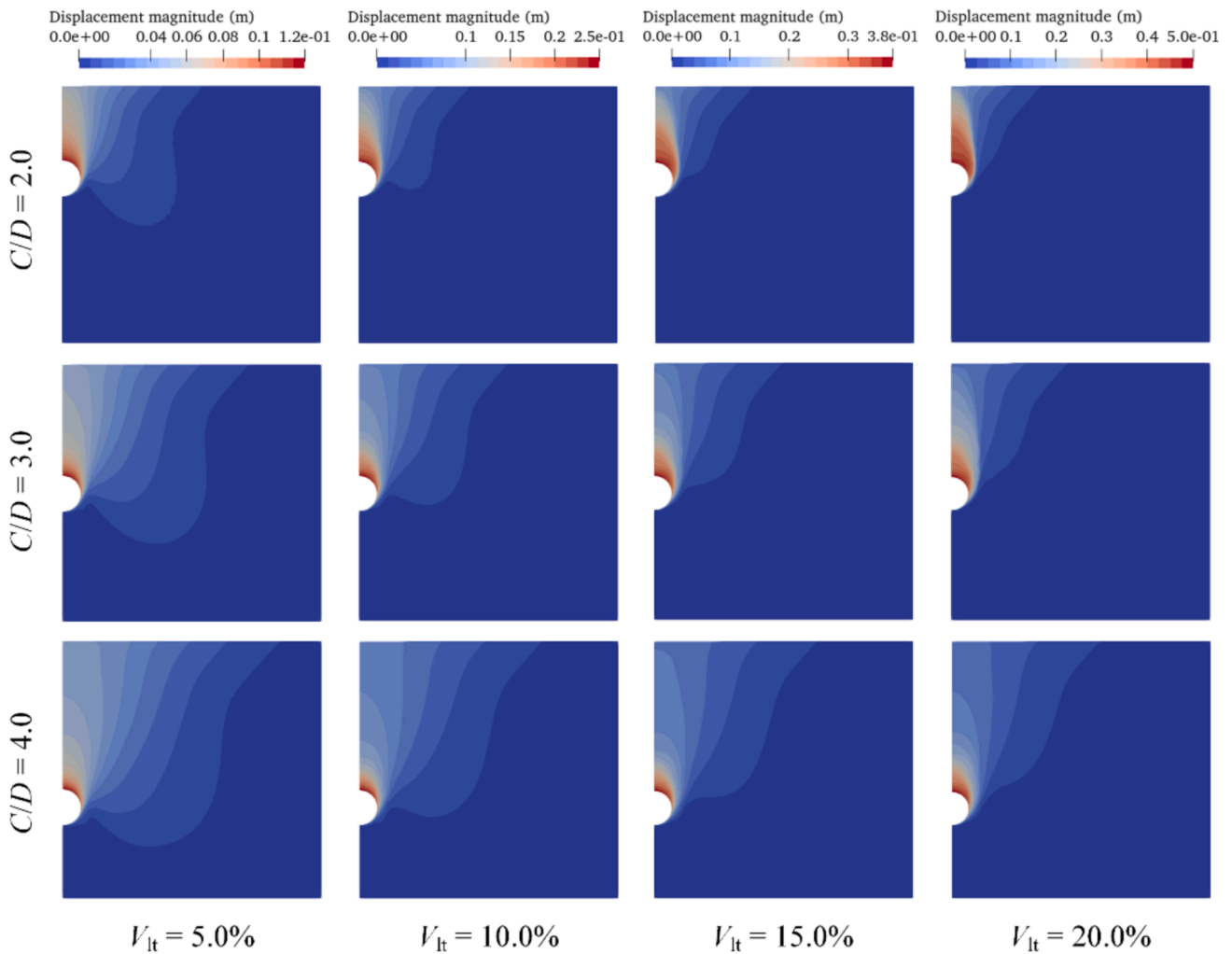


Fig. 8. Results of ground displacement with a variation of  $C/D$  and  $V_{lt}$  (Note that the max value of the color map in each  $V_{lt}$  stage is set as the maximum vertical displacements of the tunnel crown).

while the soil active region around the tunnel crown gradually extends upward. In the case of  $C/D = 2.0$ , the soil active region significantly expands from the tunnel crown to the ground surface, implying a progressive destabilization of the soil arch. However, for higher buried depths, the accelerating effect of  $V_{lt}$  on the extension of soil arching is less pronounced. Even at  $V_{lt} = 20\%$ , the active soils for  $C/D = 4.0$  remained concentrated in a localized area near the tunnel crown.

The relative movement between the active soil mass and the

surrounding ground induces a strain localization area. Fig. 9 employs the accumulated deviatoric strain to indicate the development of shear bands with increasing  $V_{lt}$  for different  $C/D$ . In the mode of eccentric volume loss, the shear bands developed from the tunnel knee, extending in the tangential direction and gradually curving. For the case of  $C/D = 2.0$ , the shear band extended vertically upward with increasing  $V_{lt}$ , and eventually curved inward and connected with the ground surface. The area encompassed by the shear bands coincides with the active soil

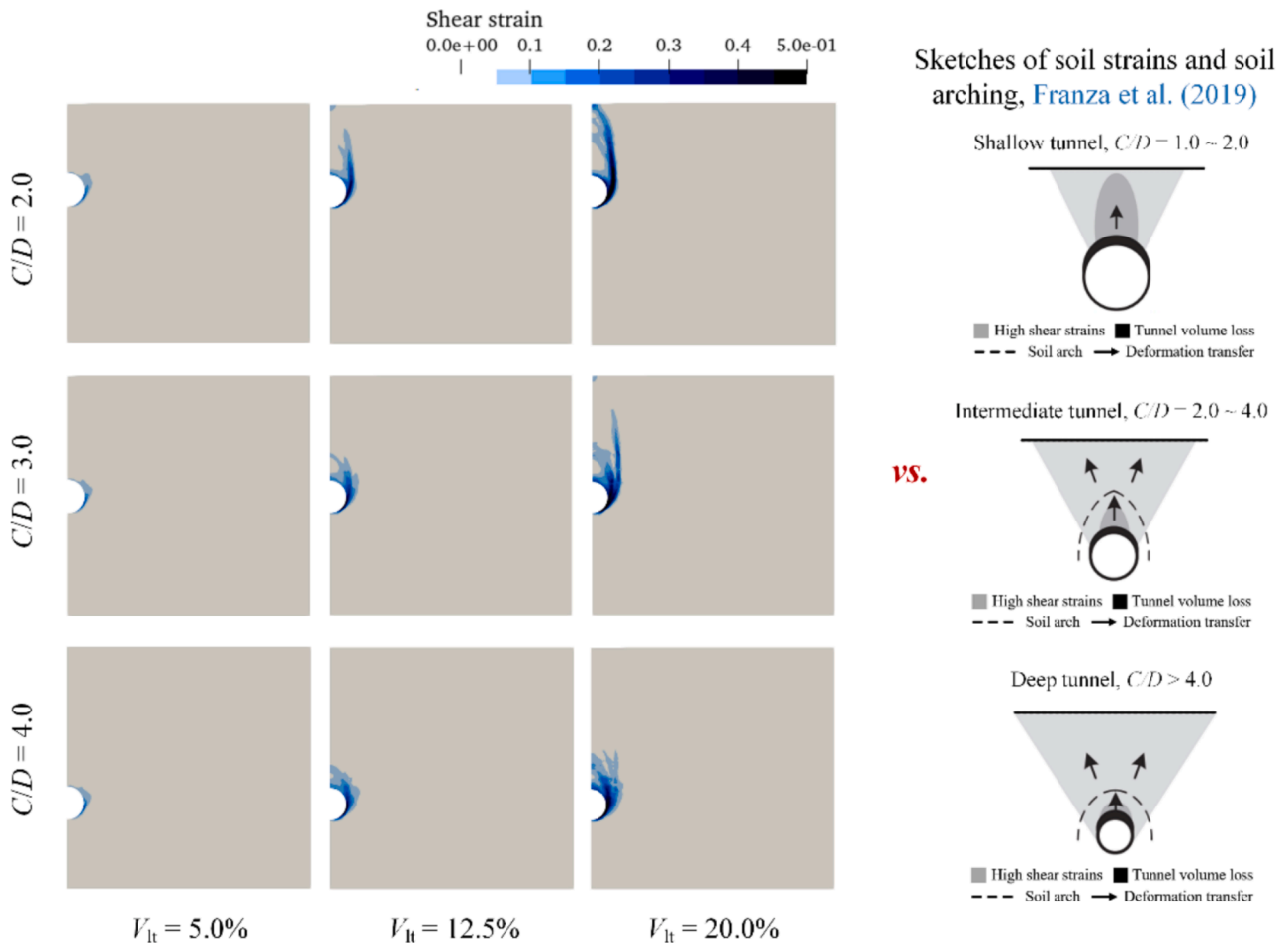


Fig. 9. Results of shear strains evolution with variation of  $C/D$  and  $V_{lt}$ , and compared with the physical test observations from Franza et al. (2019).

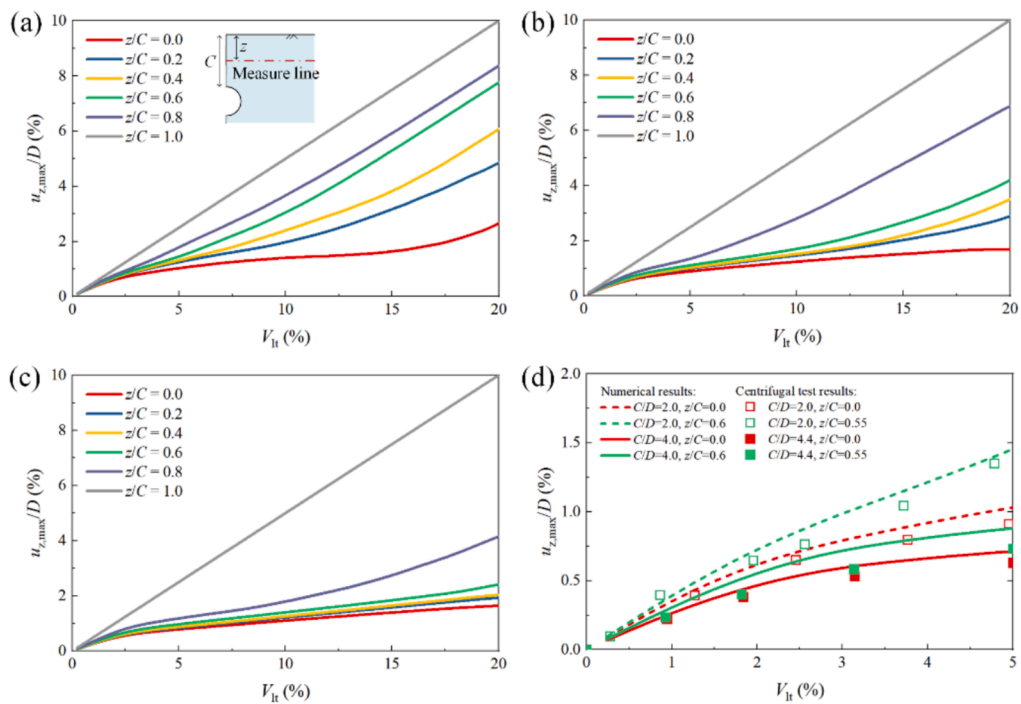


Fig. 10. Relations between maximum settlement and  $V_{lt}$  in the case of (a)  $C/D = 2.0$ , (b)  $C/D = 3.0$ , (c)  $C/D = 4.0$ , and (d) a comparison between numerical and physical test results.

region plotted in Fig. 8. The failure pattern shown in  $C/D = 2.0$  is similar to the ultimate stage illustrated in Fig. 7, and also resembles the limit equilibrium models summarized by previous studies (Lin et al., 2022c). For the case of  $C/D = 3.0$ , the shear bands firstly curved as a closed arch above the tunnel crown, implying that the active soil region was detached from the soil arch. The soil arch then partially collapsed and produced new active soil mass, triggering a new shear band developing upward with a steeper angle. For the case of  $C/D = 4.0$ , the shear band extended more slowly, indicating relatively higher stability of its soil arch. Moreover, the multiscale numerical results were qualitatively compared with the centrifugal test observations from Franza et al. (2019). The mentioned physical test utilized an approximate plane strain tunnelling test apparatus with rigid boundary control system to reproduce tunnel volume loss in an eccentric mode. These setups is similar with the numerical model setups introduced in Section 3.2. Additionally, the mentioned physical test used dense Leighton Buzzard sands, which have similar shear strength and dilatancy with the numerical CPS\_D soils, as listed in Table 2. Referring to these laboratory results, the multiscale model reproduced the strain and deformation evolution patterns in different  $C/D$  scenarios, which confirmed the reliability of the multiscale modelling approach.

The effect of soil arching on ground movement can be more clearly demonstrated by examining the relation between ground settlement and tunnel volume loss. Fig. 10 shows the maximum values of surface and subsurface settlement with increasing  $V_{It}$  for different  $C/D$ , where  $z$  represents the depth of the measure line, and the maximum settlement at  $z/C = 1.0$  represents the vertical displacement of the tunnel boundary crown. The relationship between ground settlement and  $V_{It}$  was found to be non-linear, particularly near the surface. The increase in settlement slowed down progressively with increasing  $V_{It}$  when  $V_{It} < 10\%$ , due to the formation of a soil arch that blocked the deformation transmission from the active region to the ground surface. With a further increase in  $V_{It}$ , the destabilization of the soil arch led to a re-acceleration of the ground settlement from the tunnel to the surface sequentially. For the case of  $C/D = 2.0$ , the surface settlement showed an inflection point of acceleration at  $V_{It} = 15\%$ , and at  $V_{It} = 20\%$  the settlement rate for all monitored points was almost the same as the tunnel boundary, which implies an overall sliding of the soil column above the tunnel. For deeper tunnels, the settlement acceleration was not transmitted to the surface, confirming that the soil arch is still effective. Additionally, we qualitatively compared the numerical results with the centrifugal test results in the dense Leighton Buzzard sands (Franza et al., 2019). On this basis, the ground movement in this multiscale tunneling model also exhibits a similar pattern to the centrifugal test. Nevertheless, their centrifugal test only observed the convergence trend of ground settlement in the

measured range of  $V_{It} < 5\%$ . In contrast, our multiscale model revealed the possible re-acceleration of settlement with a further increasing tunneling volume loss. For some shallow overburden tunnel cases, the delayed surface collapse in the post-construction stage (Lin et al., 2024) is similar to the evolution pattern observed in this model.

The variation of settlement trough shape with various  $C/D$  and  $V_{It}$  values is illustrated in Fig. 11(a) and (b), where the settlement value was normalized by the maximum settlement at the tunnel boundary crown. The simulated settlement trough data was well-fitted by modified Gaussian curves. In addition, a quantitative assessment of the settlement trough is also plotted in Fig. 12(a) and (b), with  $K$  representing the width parameter at various depths.  $K$  is calculated as  $i/(z_t - z)$  (where  $z$  is the measured depth and  $z_t$  is the depth of tunnel center), while  $K_s$  represents the value of  $K$  at the ground surface. Additionally, the evolution pattern of numerical results was qualitatively compared with some settlement trough data in dry dense sands (Marshall et al., 2012; Franza et al., 2019). It was observed that the settlement trough widened with increasing  $C/D$  and narrowed with increasing  $V_{It}$ . The variation patterns of the  $K$  and  $K_s$  were similar to that of the centrifugal tests, and the  $K_s$  values for different  $C/D$  were mostly within the typical value range of cohesionless soils summarized by Mair and Taylor (1997). This variation pattern reflects a progressive concentration of ground settlement towards the tunnel centerline as the increasing tunneling volume loss. In shallow tunnels, the variation gradient of  $K$  with depth was significantly lower than that in deep tunnels, and the narrowing of the settlement trough with  $V_{It}$  was more pronounced in a shallow tunnel. This implies that the soil arching above a deep tunnel acts as a more effective barrier for transforming deformation. Conversely, the ground above a shallow tunnel tends to develop a narrow, chimney-like displacement field with increasing tunneling volume loss.

#### 4.2. Effect of Soil Density and PSD on Tunneling-induced Ground Responses

The effects of soil density and PSD on ground settlement are quantitatively illustrated in Fig. 13 for the case of  $C/D = 3.0$ . CPS\_MD exhibited greater settlements and a higher settlement growth rate, with surface and subsurface settlement increasing linearly at similar rates. This differs from the settlement evolution pattern of CPS\_D, which accelerates sequentially from the tunnel to the surface in response to soil arching development. In contrast, the settlement evolution of CPG\_D closely resembled that of CPS\_D, but the mobilized ground settlement acceleration was localized within a relatively small range. It is indicated that the soil arch in dense soils plays the role of a barrier against ground deformation transfer, and the soil arch in sands is more likely to fail than

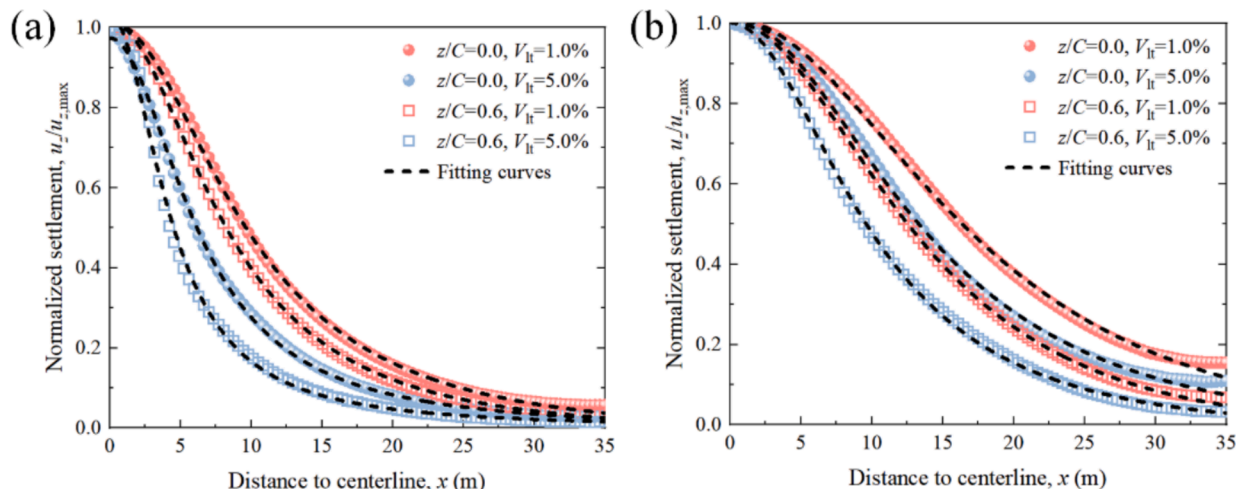


Fig. 11. Simulated settlement troughs in the cases of (a)  $C/D = 2.0$ , and (b)  $C/D = 4.0$ .

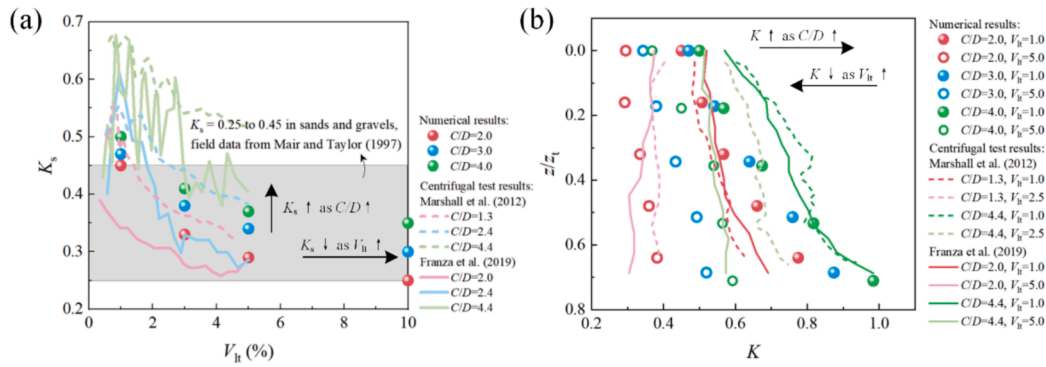


Fig. 12. Variation pattern of settlement trough width parameters of (a)  $K_s$  and (b)  $K$ .

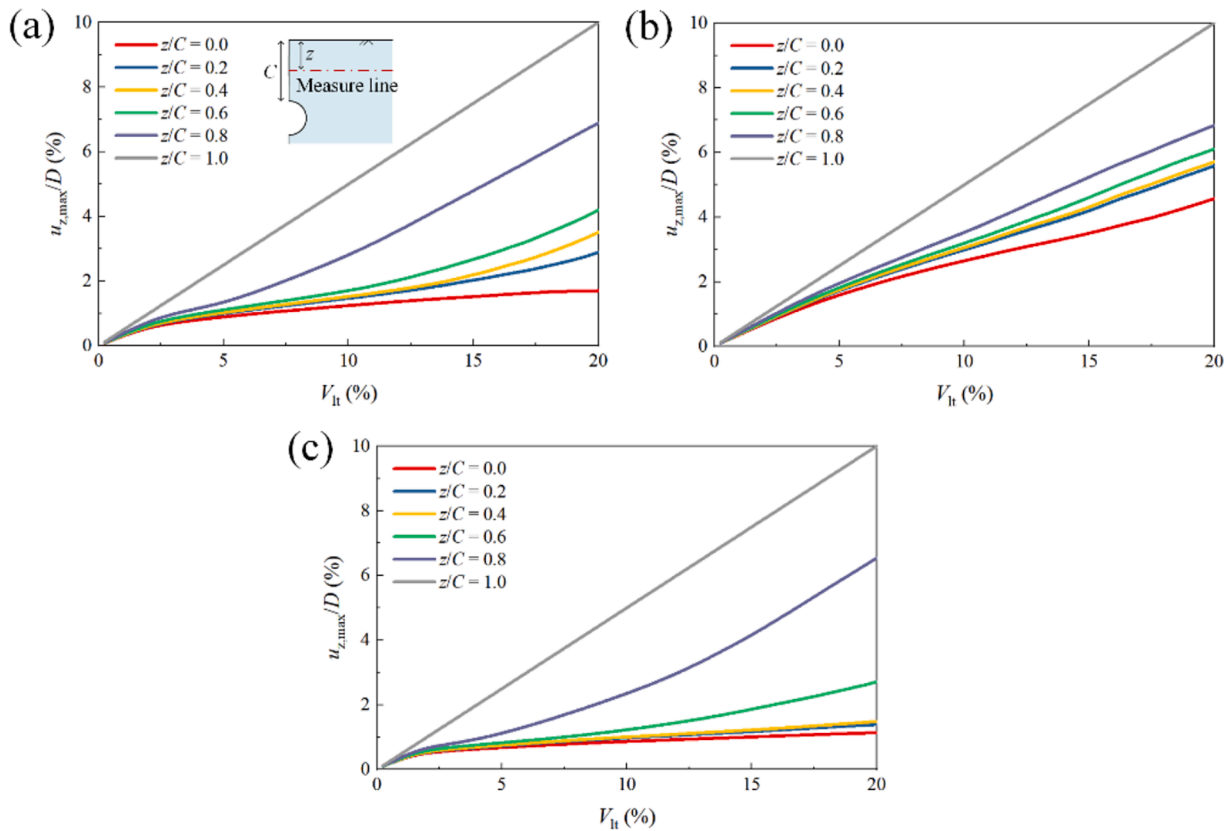


Fig. 13. Results of subsurface settlement in the case of (a) CPS\_D, (b) CPS\_MD, and (c) CPG\_D.

that in gravel soils. In contrast, soil arches in loose soils are incapable of preventing the deformation transfer from the tunnel crown to the surface.

There are also evident differences in the ground displacement and shear band patterns affected by distinct soil arching behaviors. As shown in Fig. 14, the active soil region and shear band in CPG\_D presented a parabolic shape similar to that of CPS\_D, because the active soils experienced significant displacement discontinuity from the soil arch. However, the shear band in CPG\_D did not exhibit vertically upwards extending branches, indicating greater stability of the soil arch in CPG\_D compared to CPS\_D. Conversely, more extensive active soils and upward-extending shear bands were observed in CPS\_MD, implying a more continuous upward transfer of soil deformation and eventually leading to an overall sliding of the ground above the tunnel. Notably, sketches of ground response in dense and loose sands suggested by Franza et al. (2019) are embedded in Fig. 13, which presents a high degree of agreement with the numerical results of CPS\_D and CPS\_MD.

Previous studies have found that the presence of soil arching affects the relationship between supporting pressure and volume loss in underground structures. Fig. 15 (a) illustrates a typical ground reaction curve (GRC) in a dense granular medium referring to Iglesia et al. (2014), where the overlying load first drops rapidly to a minimum due to the emergence of soil arch, and then gradually recovers to an ultimate state with the progressive destabilization of the soil arch. Referring to previous studies (Franza et al., 2019; Lin et al., 2022d), tunneling-induced soil arching can also be characterized by the relation between the vertical stress above the tunnel crown and the volume loss. Fig. 15(b) presents the tunneling-induced GRC in the multiscale model. The vertical stress value of the neighboring FEM element above the tunnel crown was recorded and normalized against its initial value before tunnelling to calculate the normalized vertical load. The GRC curve is then plotted based on the relation of the normalized vertical load with the tunnelling volume loss. Results showed that the CPS\_D and CPG\_D conform to the typical pattern shown in Fig. 15 (a). The CPG\_D exhibited

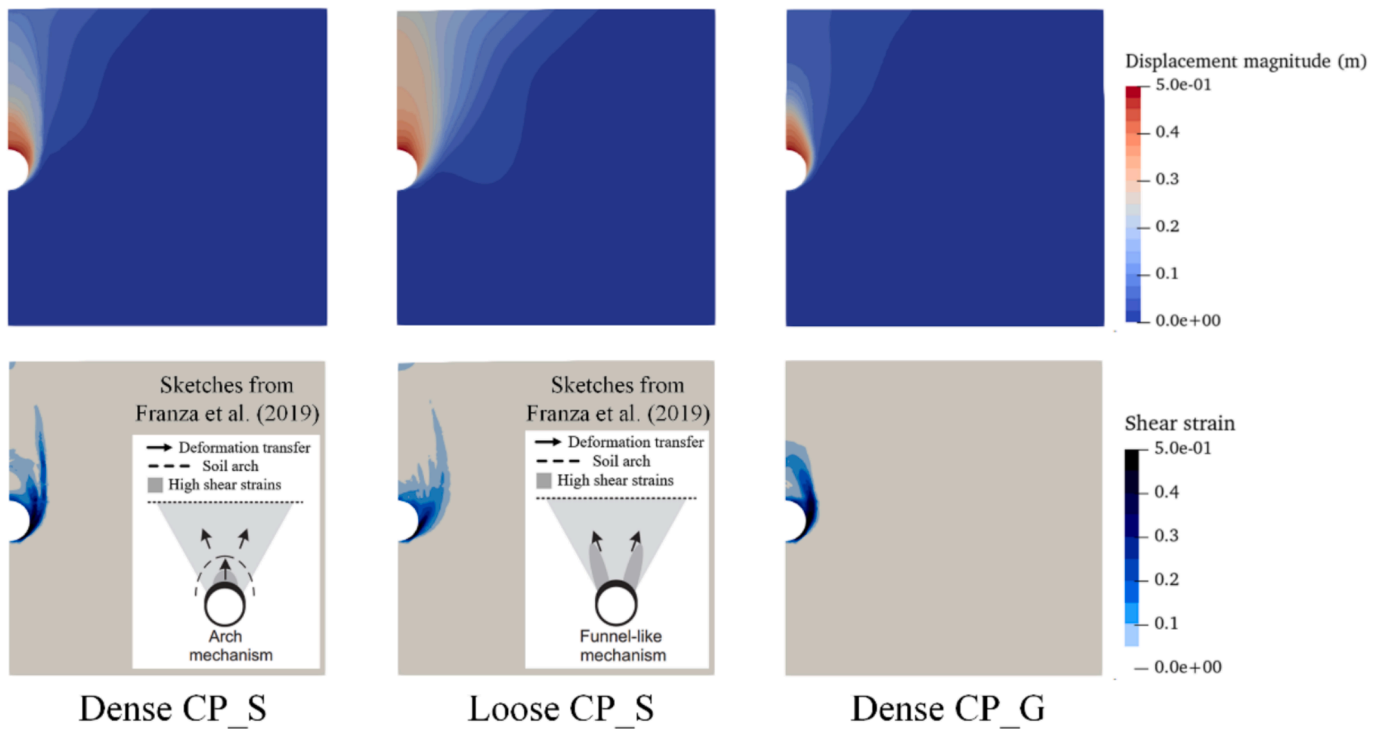


Fig. 14. Results of shear strains in different materials.

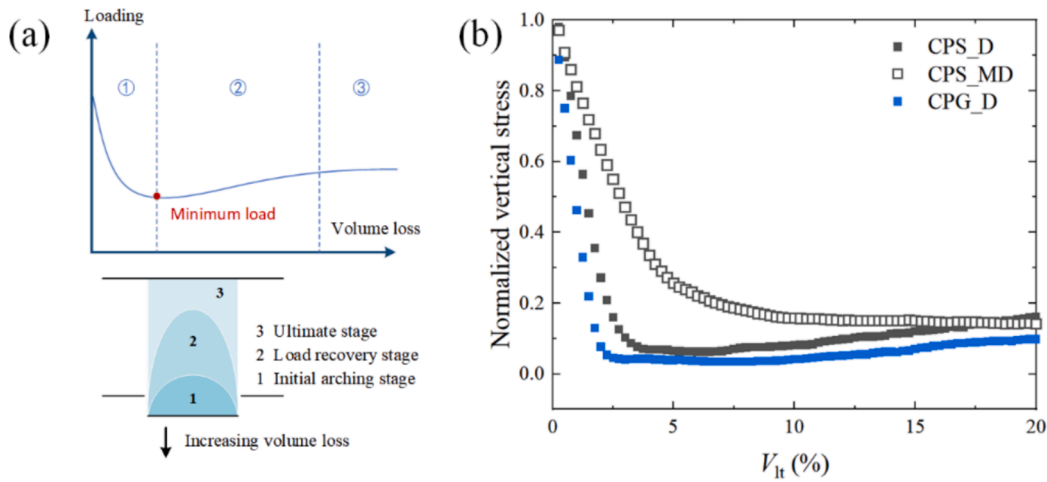


Fig. 15. GRC curves (a) illustration of typical trend and (b) simulated GRC curves for different materials.

a steeper decreasing slope, a lower minimum value, and a slower recovery compared to CPS\_D, which is consistent with observations from physical tests. (Chevalier et al., 2012) and the DEM numerical results (Xie et al., 2023). Besides, the CPS\_MD showed a slightly different GRC shape from the dense soils, where the loading did not show an evident minimum value and the recovery state, but rather decreased monotonically with tunnel volume loss and gradually converged to the ultimate state. If we characterize the GRC in dense soils as “softening”, then GRC in loose soils can be labelled as “hardening”. Referring to the evolution pattern of the soil arching shown in Figs. 13 and 14, the “hardening” and “softening” can be interpreted as the strength of the soil arch and are related to the different soil behaviour. Notably, the hardening of the GRC in the loose granular medium was also captured by previous laboratory tests (Kirsch, 2010; King et al., 2019). In the following multiscale analyses, we will discuss the mechanisms underlying the differences in soil arching evolution and GRC’s pattern.

## 5. Multiscale Analysis of Soil Arching Behavior

### 5.1. Stress Rotation and Fabric Anisotropy

In simulating the tunnel excavation process, the multiscale model accurately captured the stress variations and deviations associated with soil arching. Taking CPS\_D,  $C/D = 3.0$  as an example (as shown in Fig. 16, significant horizontal stress concentration and vertical stress reduction appeared above the tunnel with increasing tunnelling volume loss, while the tunnel sides exhibited vertical stress concentration and horizontal stress release. Moreover, Fig. 16 illustrates the major principal stress directions within the local region surrounding the tunnel. Compared to the initial gravity deposition state, the major principal stress underwent significant rotation with increasing volume loss. The major principal stress vectors above the tunnel formed continuous, upward-arching trajectories, which aligns with experimental

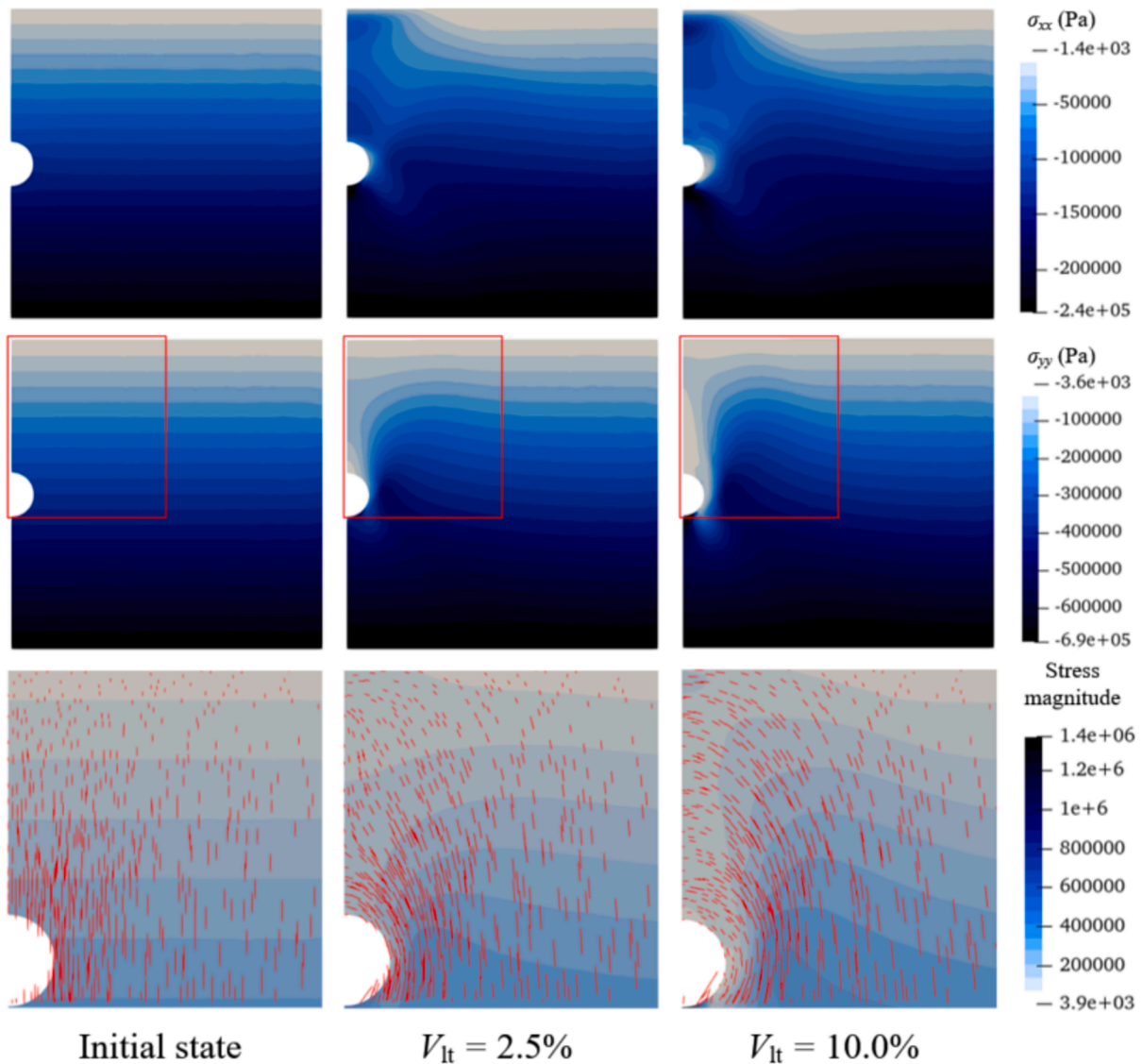


Fig. 16. Results of stress variations and major principal stress trajectories.

observations by Burke et al. (2020) and Lin et al. (2022).

To further investigate the role of microscopic fabric evolution in driving macroscopic stress rotation, three representative RVEs located along the stress rotation path (as shown in Fig. 17) were selected for visualization of the evolutions of microstructure and force chain networks. Additionally, the deformation-induced fabric anisotropy of RVEs is characterized by the distribution of contact-normal, which can be expressed as a Fourier series (Rothenburg and Bathurst, 1989)

$$E(\theta) = \frac{1}{2\pi}(1 + a\cos 2(\theta - \theta_a)) \quad (22)$$

where  $a$  is a quantity of anisotropy and  $\theta_a$  represents the principle direction of contact-normal anisotropy, and when  $a = 0$  the distribution is isotropic. As shown in Fig. 17, it is evident that all three RVEs presented significant anisotropy. Compared to the initial state under gravity deposition, the force chains at points A and B are significantly deflected. The major contact direction at point C remained vertical, but its anisotropy along the vertical direction increased significantly. The orientational distribution of normal contacts exhibited an arching pattern encircling the tunnel, demonstrating spatial concordance with the trajectories of major principal stresses. Furthermore, the fabric evolution of RVEs along the arching path provided clear elucidation of

the mechanical mechanisms underlying soil arching behavior. Under the influence of lower boundary unloading, soil particles surrounding the tunnel volume loss underwent rearrangement to form arch-shaped contact force chains. The overburden load was transmitted along these arched force chains to the tunnel sides, where the soil mass around point C functioned as an “arch foot”. The vertical unloading resulted in negligible vertical contact forces at point A, where soil stability was mainly maintained through horizontal contact forces and inter-particle friction.

The spatial correlation between the orientations of inter-particle normal contacts and major principal stress trajectory directions demonstrated the potential for predicting macroscopic soil arching phenomena through microscopic fabric characterization. To validate this predictive capability, a quantitative comparison was made between the principal stress rotation angles at specified locations (along the  $0.5D$  reference line above the tunnel crown) obtained from the FEM solver and the principal contact-normal fabric directions computed for the corresponding RVEs. As shown in Fig. 17, the rotation angle of the major principal stresses closely matches the contact-normal anisotropy directions of the RVEs. This finding demonstrated that the directional evolution of microscopic fabric anisotropy could also serve as a quantitative characterization for soil arching phenomena beyond

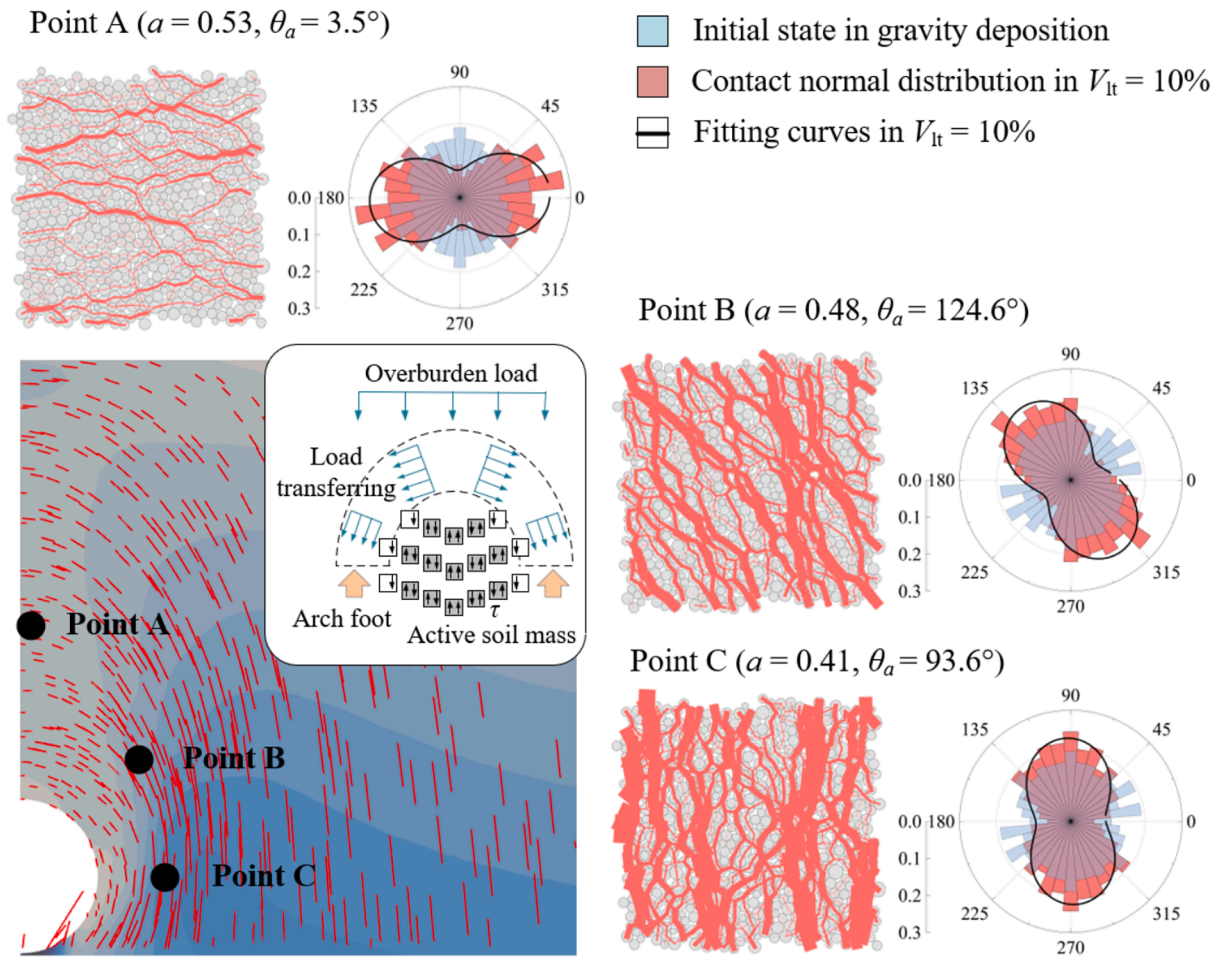


Fig. 17. Results of microstructure evolution in selected RVEs (To enhance visualization, the force-chain widths are scaled by the contact force magnitude).

macroscopic principal stress rotation.

### 5.2. RVE's Response to Soil Arch Evolution

As demonstrated in Section 4.1, with increasing tunnelling volume loss, the soil arching zone above the tunnel experienced a progressive destabilization process on a macroscopic scale. This section continues to reveal the underlying multiscale mechanical mechanisms through the investigation of RVEs' responses. Through the hierarchical multiscale method, the average particle rotation and void ratio can be measured for any Gauss point in the continuum field according to its corresponding RVE simulation. As illustrated in Fig. 19, the spatial distributions and evolution of shear strain, particle rotation, and void ratio exhibit high correlation in their localization patterns within the model of CPS\_D,  $C/D = 3.0$ , from  $V_{it} = 10\%$  to  $20\%$ . Analysis of macroscopic ground deformation patterns indicates that strain localization predominantly occurs in transition zones characterized by sharp changes in soil displacements (as shown in Figs. 8 and 9). The concentrated distribution of pronounced particle rotation demonstrates significant particle rolling and rotation in these regions, which implies relative movement between active and inactive soil masses and shear band formation at the macroscopic scale. Consistent with many laboratory observations (Oda and Kazama, 1998; Chen et al., 2021), the elevated void ratio within shear bands can be attributed to volumetric dilation induced by inter-particle climbing and rolling. This dilation response promotes soil strength degradation within strain localization zones, thereby facilitating the progressive destabilization of the soil arching region.

Taking CPS\_D,  $C/D = 3.0$  as an example, Fig. 18 shows the evolution

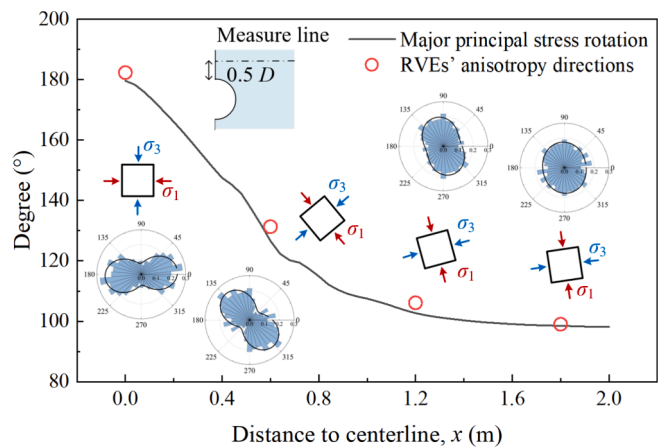


Fig. 18. Comparison between the rotation of the principal stress axis and the corresponding RVE's principal contact-normal fabric direction.

of microscopic fabric within RVEs at different locations in the soil arching zone with increasing tunnelling volume loss. From the macroscopic perspective, RVEs Aa, Ab, and Ac successively entered large deformation zones as tunnel volume loss increased. Additionally, both point Aa and point B experienced strain localization at  $V_{it} = 20\%$ . Examining the microscopic fabric response of the RVEs, with increasing soil deformation, contact forces in each RVE significantly degraded along the soil deformation direction, exhibiting progressively enhanced

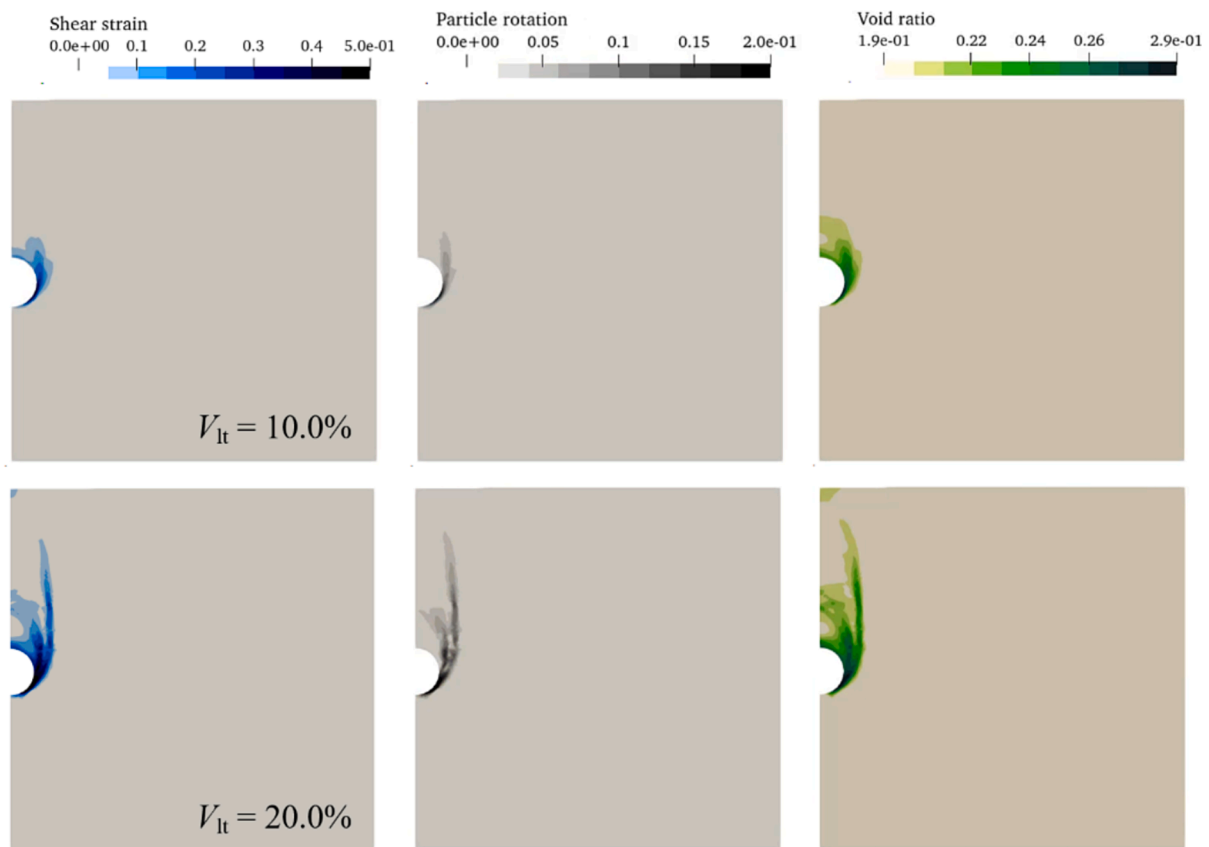


Fig. 19. Comparison between the shear strain, particle rotation and voids ratio localization.

anisotropy perpendicular to the deformation direction. From crown to ground surface, the principal directions of contact forces in RVEs Aa, Ab, and Ac rotated sequentially with increasing  $V_{lt}$ , indicating the progressive expansion of the soil arching zone. Notably, both RVE Aa and RVE B exhibited a reduction in contact forces and degradation in coordination numbers during the strain localization process. Similar microscopic structure diffusion phenomena were observed by Chen et al. (2023) in strain localization zones. The loss of contacts and highly anisotropic contact forces rendered the soil mass within strain localization zones unstable, promoting the expansion of the active soil zone and progressive destabilization of the soil arching region.

In addition, the stress–strain behaviors of RVE Aa, Ab and Ac were analyzed to further demonstrate the progressive evolution of the soil arch. According to Eqs. (7) to (11), the historical variation of deviatoric stress and volume strain for each RVE are also plotted in Fig. 21. The strain evolution in the  $x$  and  $y$  directions indicates that the RVEs within the soil arch underwent lateral contraction and vertical dilation. At the beginning of the volume loss ( $V_{lt} < 2.0\%$ ), the three RVEs experienced the unloading stage simultaneously with a linear decrease in  $q/p$ . With an increase in  $V_{lt}$ , a rapid increase in  $q/p$  first occurred in RVE Aa, which implies that the inter-particle shear resistance is activated by lateral compression. In the case that RVE Aa can hardly bear its weight and the overlying loads, significant vertical dilation occurs to compensate for the volume loss underneath. When the volume dilation reaches its critical value, the deviatoric stress of RVE Aa softens rapidly, indicating that the RVE failed from the soil arch state to the critical failure state (as described earlier, the “active soils”). Combining with Fig. 20, it is evident that RVE Aa’s volumetric dilation and softening behavior occurred during the same phase as strain localization. This provides quantitative evidence for the correlation between strain localization and soil arch destabilization. For the RVE Ab, the growth of  $q/p$  curve and dilation display a relatively gradual growth.

After the failure of RVE Aa, the deviatoric stress of RVE Ab increases to a peak value accompanied by significant volume dilation. This suggests that the soil arch at point Ab has been fully mobilized for shear resistance and is undergoing shearing deformation following the failure of RVE Aa. As for RVE Ac, the  $q/p$  curve exhibits a gentler growth pattern. When  $V_{lt} < 15\%$ , the RVE shows a volume contraction behavior, indicating that the volume change is dominated by horizontal compression. With the failure of RVE Aa, the deviatoric stress in RVE Ac also tends to peak and transition from contraction to dilation.

Moreover, Fig. 21 compares the correlation between RVE-scale stress–strain histories and the temporal evolution of macroscopic soil deformation at corresponding locations. During the linear unloading phase of deviatoric stress, macroscopic soil settlement exhibited high growth rates. As the beginning of the rapid increase in deviatoric stress, the rate of macroscopic soil settlement decreased. When deviatoric stress approached its peak value and the RVE began to demonstrate rapid volumetric dilation, macroscopic soil settlement reaccelerated. These results demonstrate the consistency between the phase evolution of soil settlement during tunnel volume loss and the stress–strain history at the RVE scale. This correlation validates the potential for predicting soil arching states through RVE-scale mechanical states: pre-peak deviatoric stress growth indicates that soil arching remains in the load-bearing phase at that location, while rapid volumetric dilation signifies soil arch destabilization.

### 5.3. Effect of Soil Density and PSD on Soil Arching

Fig. 22 compared the RVE’s responses for the soils with different densities and PSD. Compared with the CPS\_D, the deviatoric stress in CPS\_MD did not show softening behavior at all Aa, Ab, and Ac points, but increased more slowly to the peak, and the peak values were lower than that in the CPS\_D. None of these three RVEs of the CPS\_MD showed

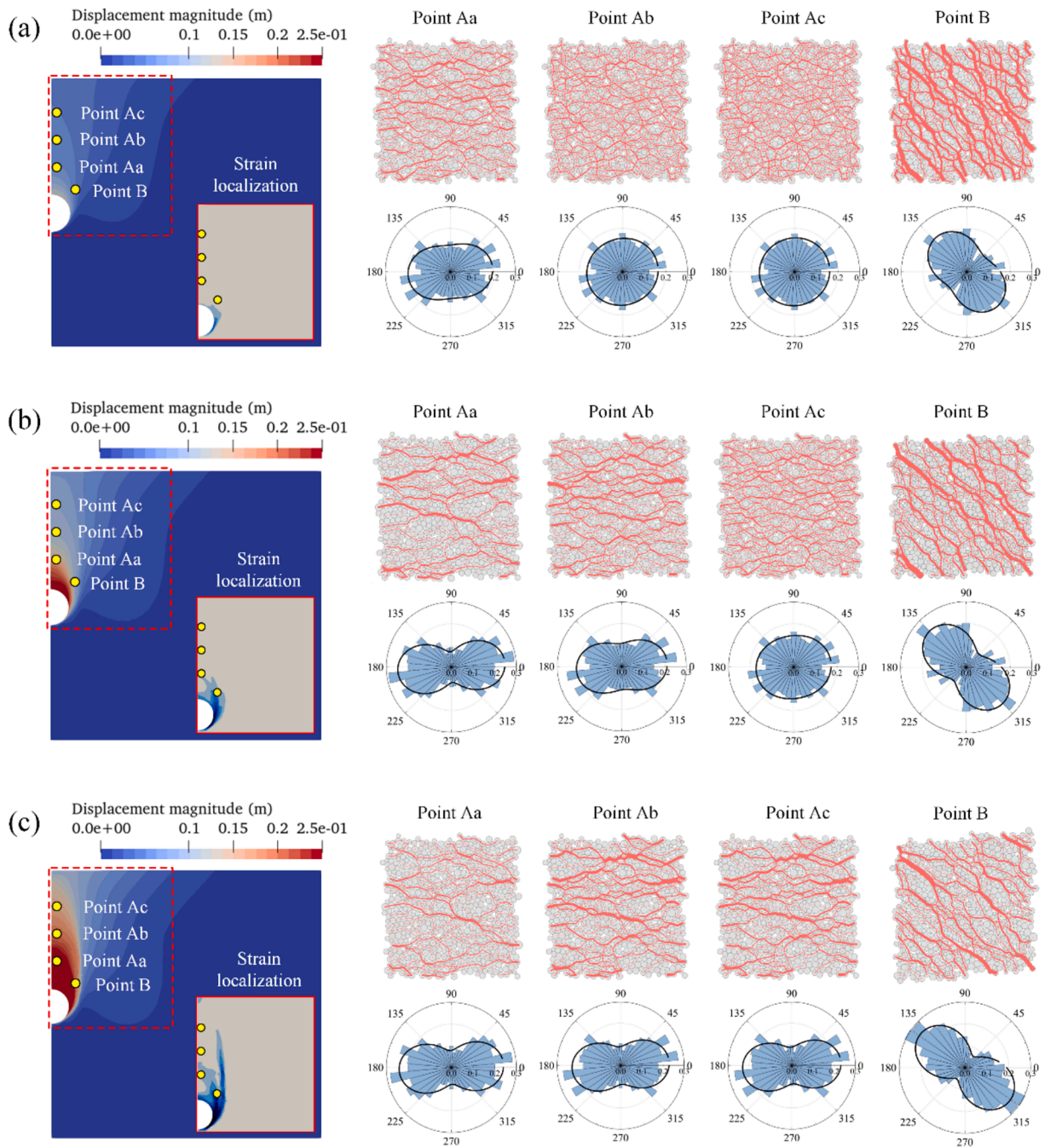


**Fig. 20.** The evolution of RVE-scale microstructure and force chains at different locations with a variation in  $V_{lt}$ , where (a)  $V_{lt} = 5.0\%$ , (b)  $V_{lt} = 12.5\%$ , and (c)  $V_{lt} = 20.0\%$ .

significant dilation behavior, instead, the RVE Ab and Ac performed significant volume contraction. For CPG\_D, the  $q/p$  curves grew to the higher peak values and persisted at the peak with no apparent softening stage, and the RVEs Aa and Ab experienced more intense dilation behaviors compared with CPS\_D.

To interpret the differences in the ground stability under different soil properties, we further examined the contact network characteristics of RVEs during arch development. The RVE located at point Aa was selected as the object of micromechanical analysis, because the soil unit at that point can undergo the complete process of soil arching leading to instability. We quantified the contact network connectivity by the mechanical coordination number, which is defined as:

$$Z_m = \frac{2N_c - N_1}{N_p - N_0 - N_1} \quad (23)$$

where  $N_c$  is the total number of contacts in a given system;  $N_p$  is the total number of particles;  $N_0$  and  $N_1$  are the number of particles with 0 and 1 contact.

As shown in Fig. 23(a),  $Z_m$  in CPS MD is significantly lower than that in the dense assemblies at the early stage of volume loss, and there is no significant difference between CPS\_D and CPG\_D. Previous studies have confirmed that particles with smaller  $Z_m$  have higher freedom for rearrangement (Liu et al., 2020), and hence the loose sand ground will experience larger deformation at the early stage of volume loss, which is in agreement with the macroscopic results observed in Fig. 13.

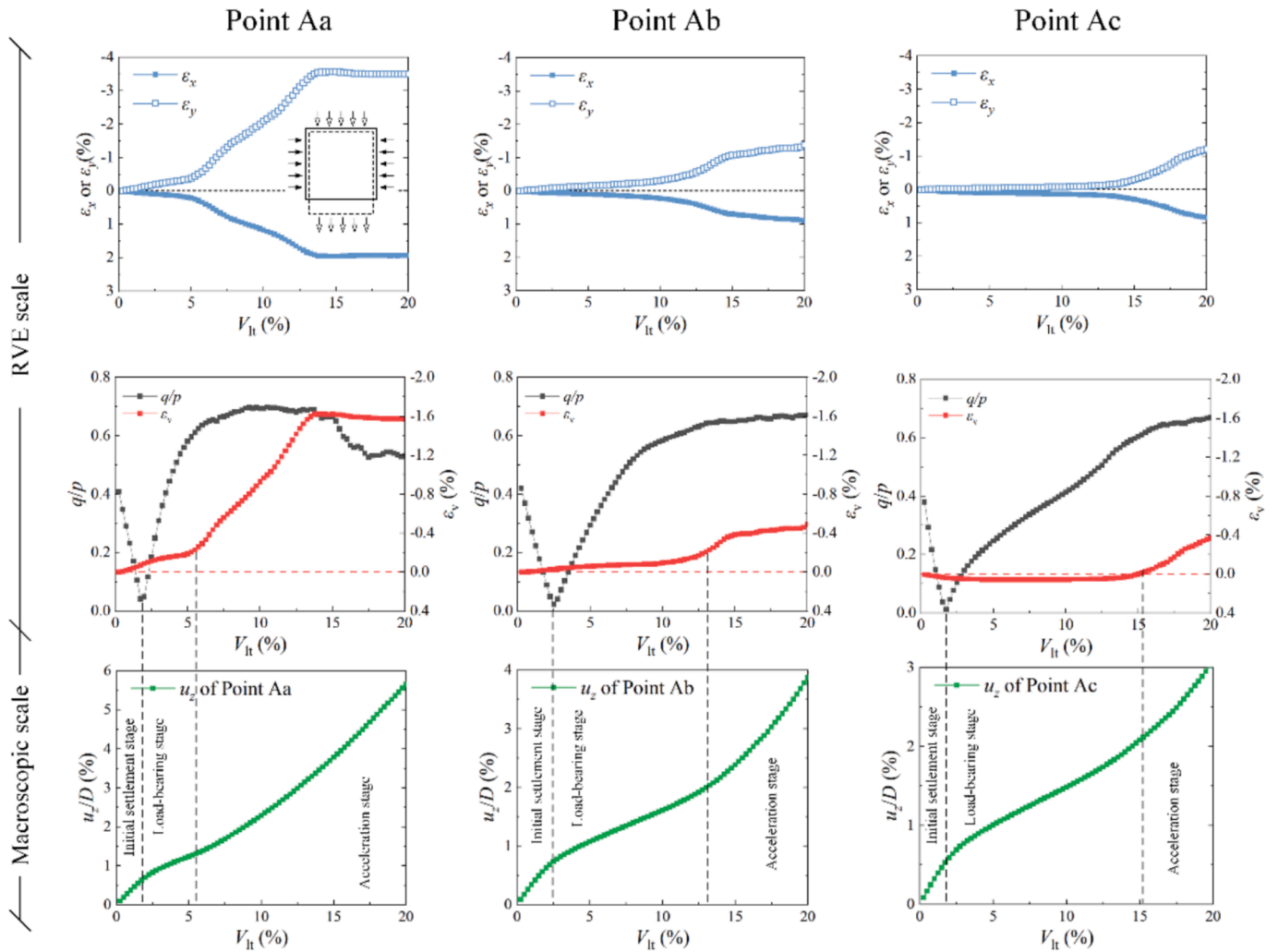


Fig. 21. Stress–strain responses in selected RVEs for the case of  $C/D = 3.0$ .

Considering the prominent contribution of the strong contact network to the overall strength of particle systems, we further quantified the connectivity of the strong contact network for CPS<sub>D</sub> and CPG. Usually, the ratio of normal contact force and their average value  $f_n/(f_n) = 1.0$  is adopted as the threshold  $\xi$  for partitioning strong and weak contacts. Moreover, we analyzed strong contact networks with higher force magnitudes of  $\xi = 2.0$  and  $\xi = 2.5$ . The connectivity of a strong contact network is also calculated via Eq. (23), where  $N_c$  and  $N_p$  represent the total numbers of strong contacts and particles involved, respectively. As shown in Fig. 23(b), the CPG consistently exhibited higher connectivity of the strong contact network throughout the tunneling-induced volume loss, especially for the sub-network with stronger contact force. The high connectivity implies that the strong contact network of CPG has more branches, serving as effective load transmission pathways, which enable better adaptation to evolving external loadings without requiring significant grain reorganizations (Muthuswamy and Tordesillas, 2006). Therefore, the soil arch in CPG ground has a greater resistance to deformation transfer compared to CPS.

Additionally, Fig. 24 visualizes the strong contact network at point Aa when  $V_{lt} = 10\%$  for different soils. The network is divided into two subsets,  $C_1$  and  $C_2$ , with  $C_2$  displaying higher contact force magnitudes. In CPG, the strong contact network spans the entire RVE system, with  $C_2$  acting as the main trunk and  $C_1$  as the branches. The strong contact network exhibits significant anisotropy along the horizontal direction. The strong contact network in CPS is much sparser, with  $C_2$  clusters

fragmentarily distributed within the RVE system. Moreover, CPS<sub>MD</sub> presented less pronounced horizontal anisotropy in the strong contacts network. In contrast, more powerful and dense horizontal contact forces are generated within the soil arch of CPG, which effectively contributes to friction and interlocking between particles to resist vertical deformation. For CPG<sub>D</sub>, we also observed that the  $C_2$  trunk in the contact network tended to pass through the coarse grains. Based on the research of Wang et al. (2023c), the coarse particles have larger inertia to oppose any motion, which can be considered as the “anchoring effect” in resisting the force chain bulking under external loadings, which essentially improves the soil arch’s stability.

## 6. Concluding remarks

This study presents a hierarchical multiscale modelling framework coupled FEM and DEM to investigate tunneling-induced ground responses in coarse-grained soils. To reproduce the engineering-scale naturally consolidated ground, a stress-controlled boundary condition is adopted to initialize the stress field for DEM RVEs. Additionally, an eccentric displacement-controlled boundary condition is presented to simulate tunneling-induced volume loss. The use of multiscale modeling enables us to discover the effect of particle-scale factors (e.g. gradation, loose or dense states of soils) on the ground deformation and failure resulting from tunneling. The numerical results in soil movement exhibit agreement with previous tests and field observations. The main findings are listed below.

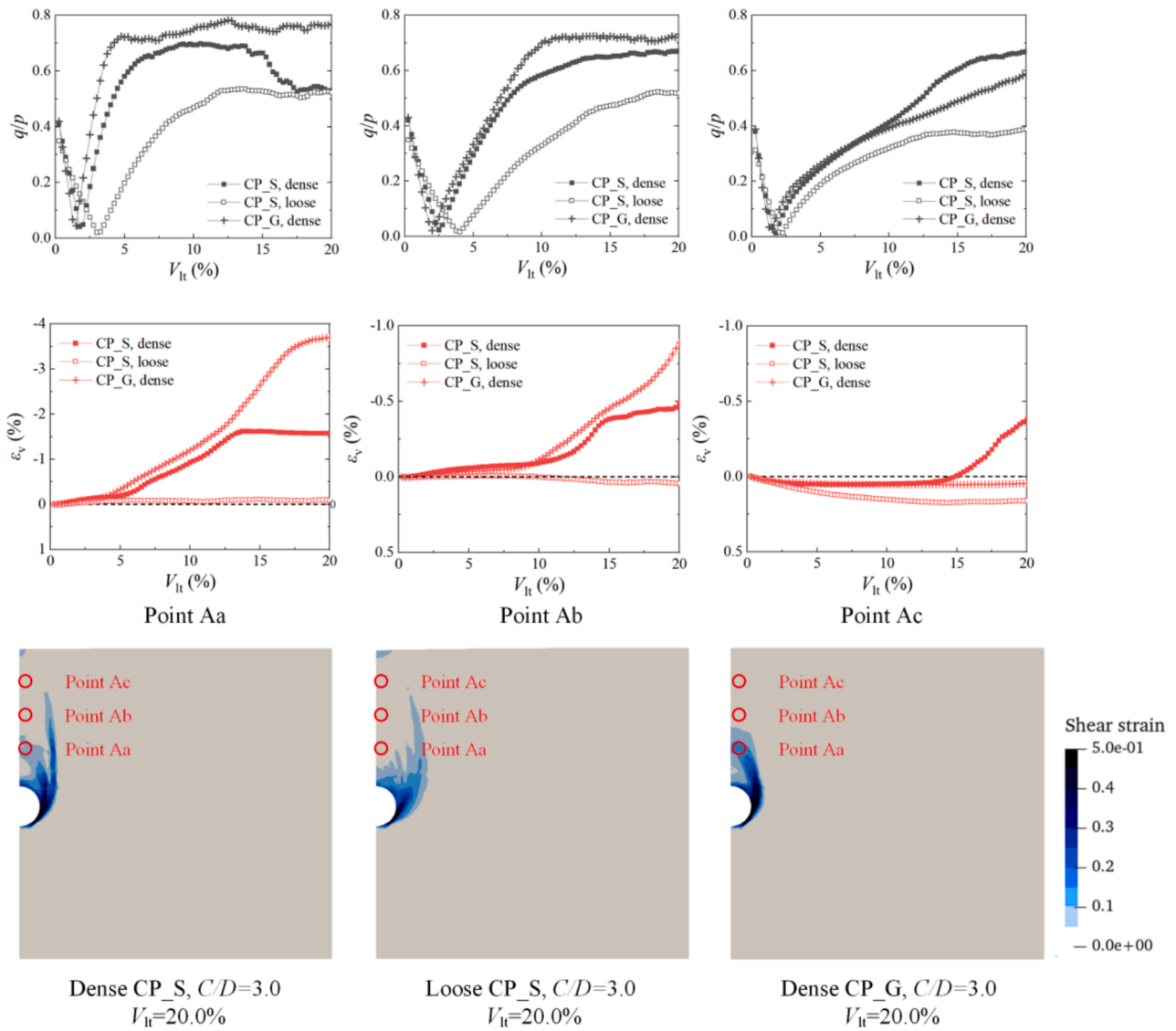


Fig. 22. Stress-strain responses in selected RVEs in different materials.

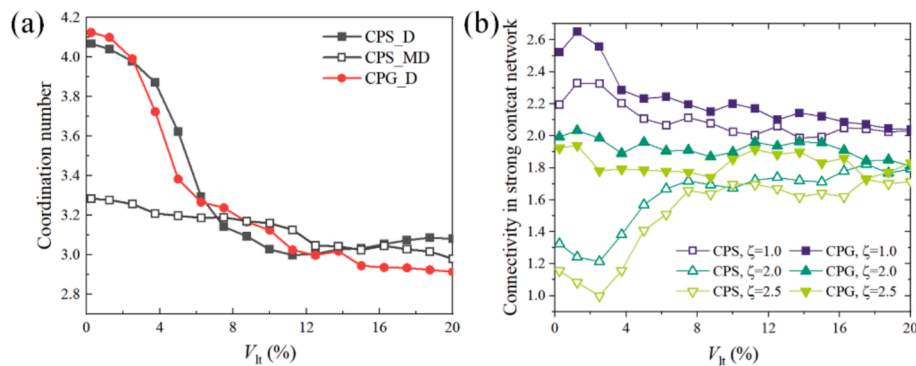


Fig. 23. Contact network comparison of: (a) coordination number between dense and loose soils; (b) strong contact network connectivity between cps and cpg.

(1) Three multiscale signatures indicating the formation and progressive development of soil arches are revealed: (i) strong force chains, (ii) the principal contact-normal fabric, and (iii) principal stress. With escalating tunnel volume loss, the directions of strong contact force chains, principal fabric, and major principal stress gradually shift and form continuous upward-arching trajectories

above the tunnel. These three indicators are interrelated and occur simultaneously. Specifically, the rotation of the principal stress and the direction of contact-normal anisotropy provide macroscopic and microscopic characterization of the soil arching trajectory, respectively.

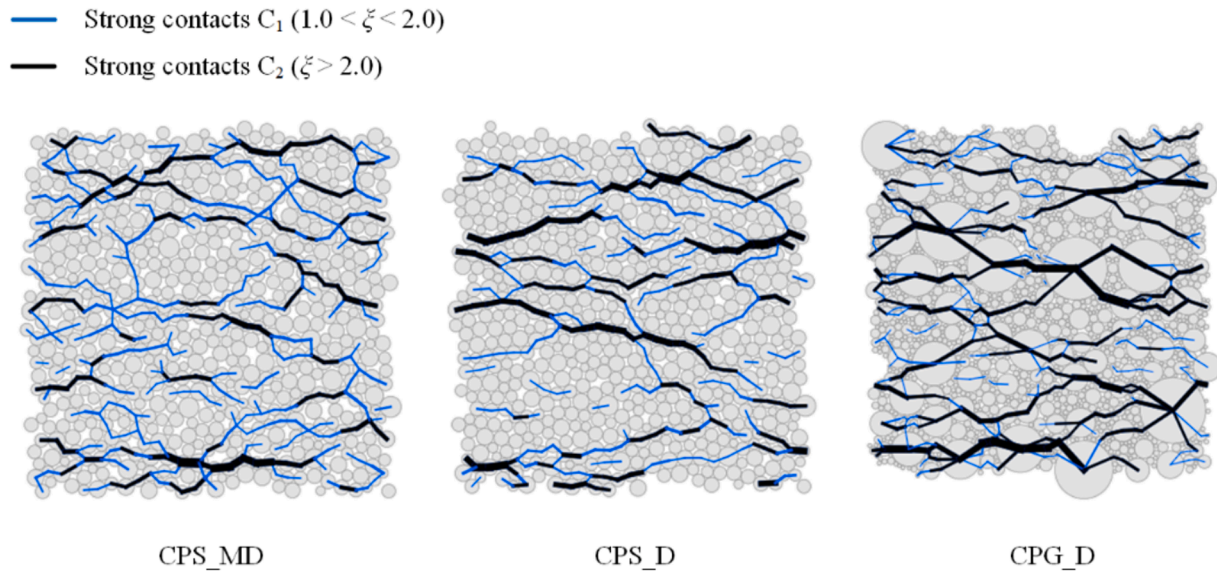


Fig. 24. Snapshots of strong contact networks at Point Aa when  $V_{It} = 10\%$ .

- (2) The hierarchical multiscale model accurately reproduces the complete evolutionary process from ground deformation to destabilization induced by tunnelling-induced volume loss. Due to the presence of soil arching, ground deformation exhibits nonlinear evolutionary characteristics. The progressive ground instability is characterized by the upward propagation of strain localization zones. The microscopic origin of progressive soil arch destabilization can be attributed to the degradation of contact forces and a reduction in coordination numbers within strain localization regions.
- (3) The tunneling-induced ground reaction curves show distinct responses in dense and loose sands. A GRC curve softening phenomenon occurs in dense sands, whereas no similar softening is observed in loose sand ground. Compared to loose soils, soil arching zones in dense soils exhibit more pronounced barrier effects against upward ground deformation transmission.
- (4) Microstructural properties significantly influence tunneling-induced ground movement in coarse-grained soils. Compared with poorly graded sands, well-graded gravels exhibit more localized ground deformation with higher soil arch stability. From the microscale perspective, the strong contact network in well-graded gravels is of high connectivity and closely anchored by coarse particles, generating robust horizontal force chains to strengthen friction and interparticle interlocking. In contrast, the weak connectivity of the contact network in loose sands leads to increased particle rearrangement and reduced capacity of the soil arch to resist vertical loading.

#### Data Availability Statement

The datasets generated during and/or analyzed during the current

study are available from the corresponding author on reasonable request.

#### CRediT authorship contribution statement

**Yipeng Xie:** Writing – original draft, Visualization, Validation, Software, Methodology, Formal analysis, Conceptualization. **Tongming Qu:** Writing – review & editing, Software, Resources, Data curation, Conceptualization. **Junsheng Yang:** Writing – review & editing, Supervision, Data curation. **Shuying Wang:** Writing – review & editing, Funding acquisition, Data curation. **Jidong Zhao:** Writing – review & editing, Supervision, Methodology, Conceptualization.

#### Declaration of competing interest

The authors declare that they have no known competing financial interests or personal relationships that could have appeared to influence the work reported in this paper.

#### Acknowledgements

This work was supported by the National Natural Science Foundation of China (Grant No. 52022112, No. 52378422 and No. 52439001). The first author thanks the team members of Prof. Jidong Zhao's Computational Granular Mechanics Lab at Hong Kong University of Science and Technology for their helpful, constructive, and convivial academic environment.

#### Appendix A. Determination of RVE Size

Referring to the guidance of [Stroeven et al. \(2004\)](#), qualitative tests on the RVE size for both CPS and CPG are documented as follows. The DEM samples for a given material are first designed as multiple testing series with different packing sizes (particle numbers). For CPS, the specimens with a particle number of 300, 500, 700, 1100, and 1500, respectively, are tested. For CPG, the specimens with a total of 1000, 1250, 1500, 2000, and 2500 particles, respectively, are tested. In each series, a total of  $n$  samples with stochastically random particle distribution are generated, and  $n = 9$  in this study. The representative capability of RVE is tested by monitoring statistical fluctuations in the biaxial mechanical responses of DEM packings. In this study, the deviatoric stress at various axial strains in sample  $i$  is considered as the tested mechanical response values  $x_i$ , and the standard deviation  $s$  is measured by

$$s^2 = \frac{1}{n-1} \sum_{i=1}^n (x_i - \bar{x})^2 \tag{A1}$$

$$\bar{x} = \frac{1}{n} \sum_{i=1}^n x_i \tag{A2}$$

where  $s$  is the sample standard deviation and  $\bar{x}$  is the sample mean. In this way the coefficient of variation  $COV$  can be derived from

$$COV = s/\bar{x} \tag{A3}$$

which expresses the fluctuation of the measured value relative to its sample average value. The smaller the  $COV$  is, the closer the sample size is to a reasonable RVE.

The deviatoric stress values at axial strains of 1 %, 2 %, 5 %, 10 %, and 20 %, respectively, in the biaxial tests for CPS\_D and CPG were selected as the examined  $x_i$ , where the  $x_i^{\varepsilon=1\%}$  and  $x_i^{\varepsilon=2\%}$  were located before the peaks of the stress–strain curve while the rests are located after the peaks. The relations between  $COV$  and the sample size are plotted in Fig. A1. The  $COV$  decreased significantly with an increasing sample size. In the case of CPS, a decrease in  $COV$  mainly occurred when the sample size increased from 300 to 700. With a further increase in the sample size, the decrease in  $COV$  is no longer significant, but the increase in the particle amounts would lead to a great increase in the computational costs. Similar results are also observed in CPG. In addition, the observed pre-peak values showed smaller  $COVs$ , while the  $COVs$  of the post-peak values fluctuated with increasing sample size after dropping to a low level, and the  $COV$  fluctuations in CPG are more apparent than CPS. This phenomenon can be attributed to the failure localization in the strain-softening stage, which leads to a lower statistical homogeneity of the softening stage compared with the hardening stage (Gitman et al., 2007; Nguyen et al., 2010).

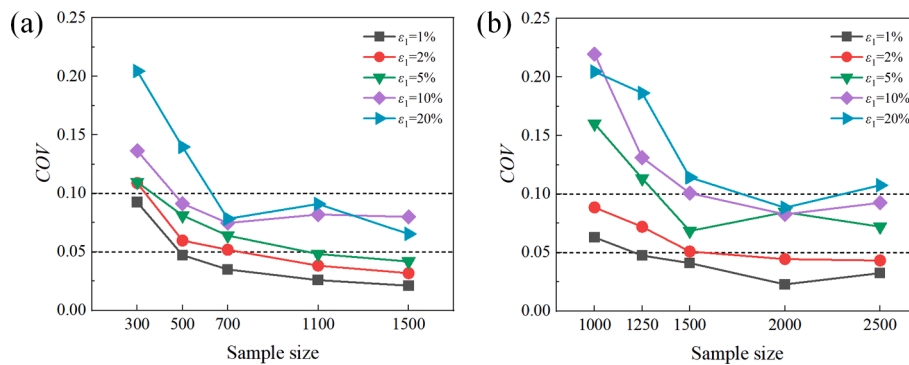


Fig. A1. Relations between  $COV$  and sample size for the case of (a) CPS and (b) CPG

In addition, the repeatability of the stress–strain response of CPS and CPG at different sizes was compared more visually in Fig. A2. The fluctuation in the stress–strain and volumetric strain curves decreased with increasing RVE sizes. Nevertheless, the average stress–strain responses for different RVE sizes show a high similarity in terms of values and curve shapes. These results prove that the RVE with different sizes is reproducible on the average level. Combined with statistical results in Fig. A1, if  $COV \leq 0.1$  is considered an acceptable target, then for CPS, a sample size with a total of 700 particles can ensure that both pre-peak and post-peak responses are adequately representative. For CPG, the acceptable RVE size is 1500 particles. The selected RVE size is higher than the usual values (size = 400) in previous 2D multiscale models (Guo and Zhao 2014; Nguyen et al. 2014; Desrues et al. 2019).

Notably, increasing the size further would slightly reduce the variability of pre-peak responses but at the cost of increased computational resources. Additionally, significant localization may occur within the RVE with an increasing size, which is suggested to be avoided by Guo and Zhao (2016). Thus, the selected RVE size strikes a balance between computational efficiency and achieving meaningful results.

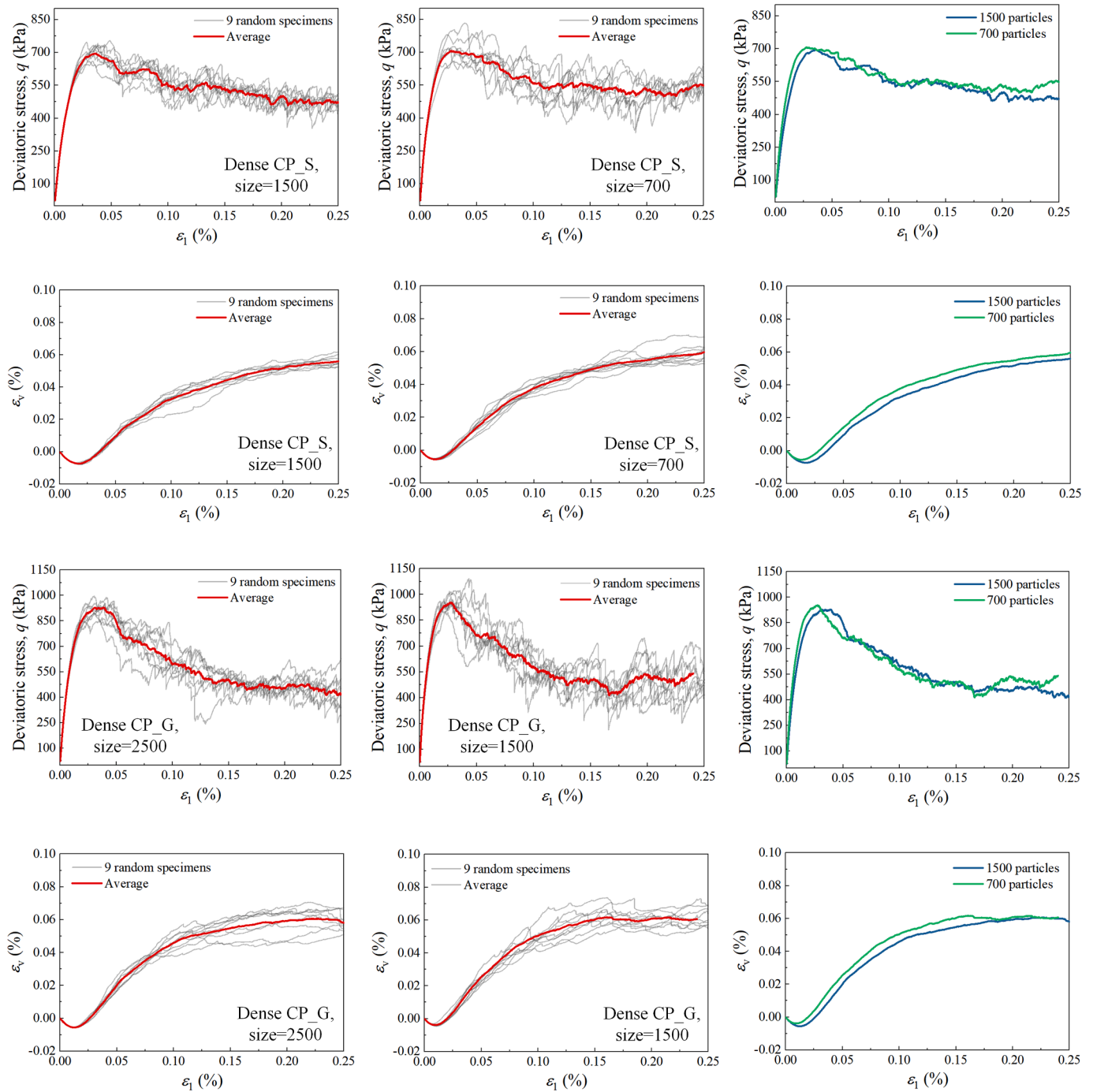


Fig. A2. Comparison of RVEs' stress-strain responses in different size

Data availability

Data will be made available on request.

References

Atkinson, J.H., Brown, E.T., Potts, D.M., 1975. Collapse of shallow unlined tunnels in dense sand. *Tunnels Tunnel.* 7 (3), 81–87.  
 Ali, U., Otsubo, M., Ebizuka, H., Kuwano, R., 2020. Particle-scale insight into soil arching under trapdoor condition. *Soils and Found.* 60 (5), 1171–1188. <https://doi.org/10.1016/j.sandf.2020.06.011>.

Alhani, I.J., Noor, M.J.B.M., Al-Bared, M.A.M., Harahap, I.S.H., Albadr, W.M., 2020. Mechanical response of saturated and unsaturated gravels of different sizes in drained triaxial testing. *Acta Geotech.* 15 (5), 3075–3093. <https://doi.org/10.1007/s11440-020-00954-4>.  
 Ahmed, S.S., Martinez, A., DeJong, J.T., 2023. Effect of gradation on the strength and stress-dilation behavior of coarse-grained soils in drained and undrained triaxial compression. *J. Geotech. Geoenviron. Eng.* 149 (5), 04023019. <https://doi.org/10.1061/JGGEFK.GTENG-10972>.  
 Bao, X., Yuan, H., Shen, J., Liu, C., Chen, X., Cui, H., 2024. Numerical analysis of seismic response of a circular tunnel-rectangular underpass system in liquefiable soil. *Computers and Geotechnics* 174, 106642.  
 Berger, K.J., Hrenya, C.M., 2014. Challenges of DEM: II. Wide particle size distributions. *Powder technology* 264, 627–633. <https://doi.org/10.1016/j.powtec.2014.04.096>.

- Boonsiri, I., Takemura, J., 2015. Observation of ground movement with existing pile groups due to tunneling in sand using centrifuge modelling. *Geotech. Geol. Eng.* 33 (1), 621–640. <https://doi.org/10.1007/s10706-015-9845-0>.
- Boldini, D., Losacco, N., Franza, A., DeJong, M.J., Xu, J., Marshall, A.M., 2021. Tunneling-induced deformation of bare frame structures on sand: numerical study of building deformations. *J. Geotech. Geoenviron. Eng.* 147 (11), 04021116. [https://doi.org/10.1061/\(ASCE\)GT.1943-5606.0002627](https://doi.org/10.1061/(ASCE)GT.1943-5606.0002627).
- Chu, J., Gan, C.L., 2004. Effect of void ratio on  $K_0$  of loose sand. *Géotechnique* 54 (4), 285–288. <https://doi.org/10.1680/geot.2004.54.4.285>.
- Chevalier, B., Combe, G., Villard, P.J.A.G., 2012. Experimental and discrete element modelling studies of the trapdoor problem: influence of the macro-mechanical frictional parameters. *Acta Geotech.* 7 (1), 15–39. <https://doi.org/10.1007/s11440-011-0152-5>.
- Chen, R.P., Tang, L.J., Yin, X.S., Chen, Y.M., Bian, X.C., 2015. An improved 3D wedge-prism model for the face stability analysis of the shield tunnel in cohesionless soils. *Acta Geotech.* 10 (2), 683–692. <https://doi.org/10.1007/s11440-014-0304-5>.
- Chen, R.P., Fu, X.S., Liu, Q.W., Wang, H.L., Meng, F., 2023a. Effect of non-simultaneous movement of adjacent twin-trapdoor on soil arching effect through discrete-element method simulation. *Transp. Geotech.* 41 (7), 101007. <https://doi.org/10.1016/j.trgeo.2023.101007>.
- Chen, Q., Gao, Y., Yuan, Q., 2021. Microstructural response during shearing process of dense sand. *Water Resources and Hydropower Engineering* 52 (6), 178–187. <https://doi.org/10.13928/j.cnki.wrahe.2021.01.022>.
- Chen, X., Shen, J., Bao, X., Wu, X., Tang, W., Cui, H., 2023b. A review of seismic resilience of shield tunnels. *Tunn. Undergr. Space Technol.* 136 (6), 105075. <https://doi.org/10.1016/j.tust.2023.105075>.
- Cheng, H., Thornton, A.R., Luding, S., Hazel, A.L., Weinhart, T., 2023. Concurrent multiscale modeling of granular materials: Role of coarse-graining in FEM-DEM coupling. *Computer Methods in Applied Mechanics and Engineering* 403, 115651. <https://doi.org/10.1016/j.cma.2022.115651>.
- Dewoolkar, M.M., Santichaiant, K., Ko, H.Y., 2007. Centrifuge modelling of granular soil response over active circular trapdoors. *Soils and Found.* 47 (5), 931–945. <https://doi.org/10.3208/sandf.47.931>.
- Desrués, J., Argilaga, A., Cailliere, D., Combe, G., Nguyen, T.K., Richefeu, V., Dal Pont, S., 2019. From discrete to continuum modelling of boundary value problems in geomechanics: An integrated FEM-DEM approach. *Int. J. Numer. Anal. Methods Geomech.* 43 (5), 919–955. <https://doi.org/10.1002/nag.2914>.
- Du, X., Zhang, P., Jin, L., Lu, D., 2019. A multi-scale analysis method for the simulation of tunnel excavation in sandy cobble stratum. *Tunn. Undergr. Space Technol.* 83 (1), 220–230. <https://doi.org/10.1016/j.tust.2018.09.019>.
- Evans, C. H., 1983. An examination of arching in granular soils. M.S. thesis, Massachusetts Institute of Technology, Cambridge, MA, USA.
- Fargnoli, V., Boldini, D., Amorosi, A., 2013. TBM tunneling-induced settlements in coarse-grained soils: The case of the new Milan underground line 5. *Tunn. Undergr. Space Technol.* 38 (9), 336–347. <https://doi.org/10.1016/j.tust.2013.07.015>.
- Fargnoli, V., Gragnano, C.G., Boldini, D., Amorosi, A., 2015. 3D numerical modelling of soil-structure interaction during EPB tunneling. *Géotechnique* 65 (1), 23–37. <https://doi.org/10.1680/geot.14.P.091>.
- Fang, X., Yang, J., Zhang, X., Zhang, C., Wang, S., Xie, Y., 2023. Numerical modeling of open TBM tunneling in stratified rock masses using a coupled FDM-DEM method. *Computers and Geotechnics* 156, 105251. <https://doi.org/10.1016/j.comptgeo.2023.105251>.
- Franza, A., Marshall, A.M., Zhou, B., 2019. Greenfield tunneling in sands: the effects of soil density and relative depth. *Géotechnique* 69 (4), 297–307. <https://doi.org/10.1680/jgeot.19.D.002>.
- Gitman, I.M., Askes, H., Sluys, L.J., 2007. Representative volume: Existence and size determination. *Eng. Fract. Mech.* 74 (16), 2518–2534. <https://doi.org/10.1016/j.engfracmech.2006.12.021>.
- Garnier, J., et al., 2007. Catalogue of scaling laws and similitude questions in geotechnical centrifuge modelling. *Int. J. Phys. Model. Geotech.* 7 (3), 01–23. <https://doi.org/10.1680/ijpmg.2007.070301>.
- Garcia, F.E., Bray, J.D., 2019. Discrete element analysis of earthquake fault rupture-soil-foundation interaction. *J. Geotech. Geoenviron. Eng.* 145 (9), 04019046. [https://doi.org/10.1061/\(ASCE\)GT.1943-5606.0002092](https://doi.org/10.1061/(ASCE)GT.1943-5606.0002092).
- Gross, L., Bourgoin, L., Hale, A.J., Mühlhau, H.B., 2007. Interface modelling in incompressible media using level sets in Escrip. *Phys. Earth Planet. Inter.* 163 (8), 23–34. <https://doi.org/10.1016/j.pepi.2007.04.004>.
- Guo, W., Tian, Z., Li, S., Shi, S., Wang, X., Li, X., 2023. Depth Effect of Rock-Breaking Seismic Source by Drilling Jumbo in Subsea Tunnel with the Drill and Blast Method and Its Application Prospects. *Journal of Marine Environmental Engineering* 11 (1), 57–77. <https://doi.org/10.32908/JMEE.v11.2023051101>.
- Guo, N., Zhao, J., 2014. A coupled FEM/DEM approach for hierarchical multiscale modelling of granular media. *Int. J. Numer. Methods Eng.* 99 (11), 789–818. <https://doi.org/10.1002/nme.4702>.
- Guo, N., Zhao, J., 2015. Multiscale insights into classical geomechanics problems. *Int. J. Numer. Anal. Methods Geomech.* 40 (3), 367–390. <https://doi.org/10.1002/nag.2406>.
- Guo, N., Zhao, J., 2016. 3D multiscale modeling of strain localization in granular media. *Comput. Geotech.* 80, 360–372. <https://doi.org/10.1016/j.comptgeo.2016.01.020>.
- Gu, X., Hu, J., Huang, M., Yang, J., 2018. Discrete element analysis of the  $K_0$  of granular soil and its relation to small strain shear stiffness. *Int. J. Geomech.* 18 (3), 06018003. [https://doi.org/10.1061/\(ASCE\)GM.1943-5622.0001102](https://doi.org/10.1061/(ASCE)GM.1943-5622.0001102).
- Guo, N., Chen, L.F., Yang, Z., 2022. Multiscale modelling and analysis of footing resting on an anisotropic sand. *Géotechnique* 72 (4), 364–376. <https://doi.org/10.1680/jgeot.20.P.306>.
- Gong, J., Pang, X., Tang, Y., Liu, M., Jiang, J., Ou, X., 2024. Effects of particle shape, physical properties and particle size distribution on the small-strain stiffness of granular materials: A DEM study. *Comput. Geotech.* 165, 105903. <https://doi.org/10.1016/j.comptgeo.2023.105903>.
- Hagiwara, T., Grant, R.J., Calvello, M., Taylor, R.N., 1999. The effect of overlying strata on the distribution of ground movements induced by tunneling in clay. *Soils Found.* 39 (3), 63–73. <https://doi.org/10.3208/sandf.39.3.63>.
- Hu, X., He, C., Walton, G., Fang, Y., Dai, G., 2020. Laboratory model test of EPB shield tunneling in a cobble-rich soil. *J. Geotech. Geoenviron. Eng.* 146 (10), 04020112. [https://doi.org/10.1061/\(ASCE\)GT.1943-5606.0002355](https://doi.org/10.1061/(ASCE)GT.1943-5606.0002355).
- Hu, X., He, C., Walton, G., Fang, Y., 2021. Face failure in cobble-rich soil: Numerical and experimental approaches on 1g EPB reduced scale model. *Soils Found.* 61 (6), 1500–1528. <https://doi.org/10.1016/j.sandf.2021.08.008>.
- Hu, Z., Yang, Z., Guo, N., Zhang, Y., 2022. Multiscale modeling of seepage-induced suffusion and slope failure using a coupled FEM-DEM approach. *Comput. Methods Appl. Mech. Eng.* 398 (8), 115177. <https://doi.org/10.1016/j.cma.2022.115177>.
- Iwashita, K., Oda, M., 1998. Rolling resistance at contacts in simulation of shear band development by DEM. *J. Eng. Mech.* 124 (3), 285–292. [https://doi.org/10.1061/\(ASCE\)0733-9399\(1998\)124:3\(285\)](https://doi.org/10.1061/(ASCE)0733-9399(1998)124:3(285)).
- Iglesia, G.R., Einstein, H.H., Whitman, R.V., 1999. Determination of vertical loading on underground structures based on an arching evolution concept. In: Proc., 3rd National Conf. on Geo-Engineering for Underground Facilities. ASCE, Reston, VA, pp. 495–506.
- Iglesia, G.R., Einstein, H.H., Whitman, R.V., 2014. Investigation of soil arching with centrifuge tests. *J. Geotech. Geoenviron. Eng.* 140 (2), 04013005. [https://doi.org/10.1061/\(ASCE\)GT.1943-5606.0000998](https://doi.org/10.1061/(ASCE)GT.1943-5606.0000998).
- Kozicki, J., Donze, F.V., 2009. YADE-OPEN DEM: An open-source software using a discrete element method to simulate granular material. *Eng. Comput.* 26 (10), 786–805. <https://doi.org/10.1108/02644400910985170>.
- Kirsch, A., 2010. Experimental investigation of the face stability of shallow tunnels in sand. *Acta Geotech.* 5 (3), 43–62. <https://doi.org/10.1007/s11440-010-0110-7>.
- King, L., Bouazza, A., Dubsy, S., Rowe, R.K., Gniel, J., Bui, H.H., 2019. Kinematics of soil arching in piled embankments. *Géotechnique* 69 (11), 941–958. <https://doi.org/10.1680/jgeot.18.P.104>.
- Loganathan, N., Poulos, H.G., 1998. Analytical prediction for tunneling-induced ground movements in clays. *J. Geotech. Geoenviron. Eng.* 124 (9), 846–856. [https://doi.org/10.1061/\(ASCE\)1090-0241\(1998\)124:9\(846\)](https://doi.org/10.1061/(ASCE)1090-0241(1998)124:9(846)).
- Loganathan, N., Poulos, H.G., Stewart, D.P., 2000. Centrifuge model testing of tunneling induced ground and pile deformations. *Géotechnique* 50 (3), 283–294. <https://doi.org/10.1680/geot.2000.50.3.283>.
- Lee, C.J., Chiang, K.H., Kuo, C.M., 2004. Ground movement and tunnel stability when tunneling in sandy ground. *J. Chin. Inst. Eng.* 27 (7), 1021–1032. <https://doi.org/10.1080/02533839.2004.9670957>.
- Lee, Y.J., 2009. Investigation of subsurface deformations associated with model tunnels in a granular mass. *Tunn. Undergr. Space Technol.* 24 (6), 654–664. <https://doi.org/10.1016/j.tust.2009.07.001>.
- Lanzano, G., Visone, C., Bilotta, E., Santucci de Magistris, F., 2016. Experimental assessment of the stress-strain behaviour of Leighton Buzzard sand for the calibration of a constitutive model. *Geotech. and Geol. Eng.* 34, 991–1012. <https://doi.org/10.1007/s10706-016-0019-5>.
- Liu, J., Zhou, W., Ma, G., Yang, S., Chang, X., 2020. Strong contacts, connectivity and fabric anisotropy in granular materials: a 3D perspective. *Powd. Technol.* 366, 747–760. <https://doi.org/10.1016/j.powtec.2020.03.018>.
- Lin, Q., Lu, D., Lei, C., Tian, Y., Gong, Q., Du, X., 2021. Model test study on the stability of cobble strata during shield under-crossing. *Tunn. Undergr. Space Technol.* 110 (4), 103807. <https://doi.org/10.1016/j.tust.2020.103807>.
- Lin, Q., Lu, D., Lei, C., Tian, Y., Kong, F., Du, X., 2022a. Mechanical response of existing tunnels for shield under-crossing in cobble strata based on the model test. *Tunn. Undergr. Space Technol.* 125 (7), 104505. <https://doi.org/10.1016/j.tust.2022.104505>.
- Lin, X.T., Chen, R.P., Wu, H.N., Meng, F.Y., Liu, Q.W., Su, D., 2022b. A composite function model for predicting the ground reaction curve on a trapdoor. *Comput. Geotech.* 141 (1), 104496. <https://doi.org/10.1016/j.comptgeo.2021.104496>.
- Lin, X.T., Chen, R.P., Wu, H.N., Meng, F.Y., Su, D., Han, K., 2022c. Calculation of earth pressure distribution on the deep circular tunnel considering stress-transfer mechanisms in different zones. *Tunn. Undergr. Space Technol.* 119 (1), 104211. <https://doi.org/10.1016/j.tust.2021.104211>.
- Lin, X.T., Su, D., Shen, X., Peng, Y., Han, K., Chen, X., 2022d. Effect of tunnelling-induced ground loss on the distribution of earth pressure on a deep underground structure. *Comput. Geotech.* 147, 104781. <https://doi.org/10.1016/j.comptgeo.2022.104781>.
- Lin, Q., Lu, D., Guo, C., Li, X., Zhao, Z., Du, X., 2024. Collapse behavior and mechanical response of the cobble stratum during the shield driving. *Tunn. Undergr. Space Technol.* 144, 105507. <https://doi.org/10.1016/j.tust.2023.105507>.
- Liu, Q., Wang, H., Chen, R., Yin, Z., Lin, X., Wu, H., 2022. Effect of relative density of 2D granular materials on the arching effect through numerical trapdoor tests. *Comput. Geotech.* 141 (1), 104553. <https://doi.org/10.1016/j.comptgeo.2021.104553>.
- Mair, R. J., Taylor, R. N., 1997. Bored tunneling in the urban environment. In: Proc., 14th Int. Conf. Soil Mech. Found. Eng., Hamburg 4, 2353–2385.
- Muthuswamy, M., Tordesillas, A., 2006. How do interparticle contact friction, packing density and degree of polydispersity affect force propagation in particulate assemblies? *Journal of Statistical Mechanics: Theory and Experiment* 2006 (09), P09003. <https://doi.org/10.1088/1742-5468/2006/09/P09003>.
- Migliazza, M., Chiorboli, M., Giani, G.P., 2009. Comparison of analytical method, 3D finite element model with experimental subsidence measurements resulting from the extension of the Milan underground. *Comput. Geotech.* 36 (1–2), 113–124. <https://doi.org/10.1016/j.comptgeo.2008.03.005>.

- Marshall, A.M., Farrell, R.P., Klar, A., Mair, R., 2012. Tunnels in sands: the effect of size, depth and volume loss on greenfield displacements. *Géotechnique* 62 (5), 385–399. <https://doi.org/10.1680/geot.10.P.047>.
- Mourlas, C., Pardoën, B., Bésuelle, P., 2023. Large-scale failure prediction of clay rock from small-scale damage mechanisms of the rock medium using multiscale modelling. *International Journal for Numerical and Analytical Methods in Geomechanics* 47 (7), 1254–1288. <https://doi.org/10.1002/nag.3513>.
- Nomoto, T., Imamura, S., Hagiwara, T., Kusakabe, O., Fujii, N., 1999. Shield tunnel construction in centrifuge. *J. Geotech. Geoenviron. Eng.* 125 (4), 289–300. [https://doi.org/10.1061/\(ASCE\)1090-0241\(1999\)125:4\(289\)](https://doi.org/10.1061/(ASCE)1090-0241(1999)125:4(289)).
- Nguyen, V.P., Lloberas Valls, O., Stroeven, M., Sluys, L.J., 2010. On the existence of representative volumes for softening quasi-brittle materials - A failure zone averaging scheme. *Comput. Methods Appl. Mech. Eng.* 199 (45–48), 3028–3038. <https://doi.org/10.1016/j.cma.2010.06.018>.
- Nguyen, H.B.K., Rahman, M.M., Fourie, A.B., 2017. Undrained behaviour of granular material and the role of fabric in isotropic and K 0 consolidations: DEM approach. *Géotechnique* 67 (2), 153–167. <https://doi.org/10.1680/jgeot.15.P.234>.
- Nurul Islam, M., Siddika, A., Belal Hossain, M., Rahman, A., Abdullah Asad, M., 2011. Effect of particle size on the shear strength behaviour of sands. *Aust. Geomech.* 46 (3), 75–86. <https://doi.org/10.48550/arXiv.1902.09079>.
- Nguyen, T.K., Combe, G., Caillerie, D., Desrués, J., 2014. FEM × DEM modelling of cohesive granular materials: Numerical homogenization and multi-scale simulations. *Acta Geophys.* 62 (5), 1109–1126. <https://doi.org/10.2478/s11600-014-0228-3>.
- Napoli, M.L., Barbero, M., Scavia, C., 2021. Tunneling in heterogeneous rock masses with a block-in-matrix fabric. *Int. J. Rock Mech. Min. Sci.* 138 (2), 104655. <https://doi.org/10.1016/j.ijrmm.2021.104655>.
- Qu, T., Wang, S., Fu, J., Hu, Q., Zhang, X., 2019. Numerical examination of EPB shield tunneling-induced responses at various discharge ratios. *J. Perform. Constr. Facil.* 33 (3), 04019035. [https://doi.org/10.1061/\(ASCE\)CF.1943-5509.0001300](https://doi.org/10.1061/(ASCE)CF.1943-5509.0001300).
- Qu, T., Feng, Y., Wang, M., 2021a. An adaptive granular representative volume element model with an evolutionary periodic boundary for hierarchical multiscale analysis. *Int. J. Numer. Methods Eng.* 122 (9), 2239–2253. <https://doi.org/10.1002/nme.6620>.
- Qu, T., Di, S., Feng, Y.T., Wang, M., Zhao, T., 2021b. Towards data-driven constitutive modelling for granular materials via micromechanics-informed deep learning. *Int. J. Plast.* 144 (9), 103046. <https://doi.org/10.1016/j.ijplas.2021.103046>.
- Qu, T., Wang, M., Feng, Y., 2022. Applicability of discrete element method with spherical and clumped particles for constitutive study of granular materials. *J. Rock Mech. Geotech. Eng.* 14 (1), 240–251. <https://doi.org/10.1016/j.jrmge.2021.09.015>.
- Rothenburg, L., Bathurst, R.J., 1989. Analytical study of induced anisotropy in idealized granular materials. *Géotechnique* 39 (4), 601–614. <https://doi.org/10.1680/geot.1989.39.4.601>.
- Stone, K.J., Wood, D.M., 1992. Effects of dilatancy and particle size observed in model tests on sand. *Soils and Found.* 32 (4), 43–57. <https://doi.org/10.3208/sandf1972.32.4.43>.
- Schanz, T., Vermeer, P.A., 1996. Angles of friction and dilatancy of sand. *Géotechnique* 46 (1), 145–151. <https://doi.org/10.1680/geot.1996.46.1.145>.
- Stroeven, M., Askes, H., Sluys, L., 2004. Numerical determination of representative volumes for granular materials. *Comput. Methods Appl. Mech. Eng.* 193 (30–32), 3221–3238. <https://doi.org/10.1016/j.cma.2003.09.023>.
- Song, G., Marshall, A.M., 2020. Centrifuge modelling of tunneling induced ground displacements: pressure and displacement control tunnels. *Tunn. Undergr. Space Technol.* 103 (9), 103461. <https://doi.org/10.1016/j.tust.2020.103461>.
- Song, S., Wang, P., Yin, Z., Cheng, Y.P., 2024. Micromechanical modeling of hollow cylinder torsional shear test on sand using discrete element method. *Journal of Rock Mechanics and Geotechnical Engineering*. <https://doi.org/10.1016/j.jrmge.2024.02.010>.
- Shao, X., Yang, Z., Jiang, Y., Feng, J., 2022. Coupled FDM–DEM Method for Analyzing EPBS Machine Tunneling Performance in Boulders. *Int. J. Geomech.* 22 (12), 04022239. [https://doi.org/10.1061/\(ASCE\)GM.1943-5622.0002594](https://doi.org/10.1061/(ASCE)GM.1943-5622.0002594).
- Shen, J., Bao, X., Cui, H., Chen, X., 2022. Experimental investigation on the relationship between influence factors of liquefaction and microstructural characteristics of muddy sand. *Constr. Build. Mater.* 324 (3), 126619. <https://doi.org/10.1016/j.conbuildmat.2022.126619>.
- Terzaghi, K., 1936. Stress distribution in dry sand and in saturated sand above a yielding trap door. In: Proc., First Int. Conf. on Soil Mechanics and Foundation Engineering, International Society for Soil Mechanics and Geotechnical Engineering, pp. 307–311.
- Terzaghi, K., 1943. *Theoretical soil mechanics*. Wiley, New York.
- Vardoulakis, L., Graf, B., Gudehus, G., 1981. Trap-door problem with dry sand: A statical approach based upon model test kinematics. *Int. J. Numer. Anal. Methods Geomech.* 5 (1), 57–78. <https://doi.org/10.1002/nag.1610050106>.
- Vorster, T.E., Klar, A., Soga, K., Mair, R.J., 2005. Estimating the effects of tunneling on existing pipelines. *J. Geotech. Geoenviron. Eng.* 131 (11), 1399–1410. [https://doi.org/10.1061/\(ASCE\)1090-0241\(2005\)131:11\(1399\)](https://doi.org/10.1061/(ASCE)1090-0241(2005)131:11(1399)).
- Vu, M.N., Broere, W., Bosch, J., 2016. Volume loss in shallow tunneling. *Tunn. Undergr. Space Technol.* 59, 77–90. <https://doi.org/10.1016/j.tust.2016.06.011>.
- Wu, H., Zhao, J., Guo, N., 2018. Multiscale insights into borehole instabilities in high-porosity sandstones. *J. Geophys. Res. Solid Earth* 123 (5), 3450–3473. <https://doi.org/10.1029/2017JB015366>.
- Wang, D., He, S., Liu, X., Li, C., Zhang, J., 2019. A modified method for determining the overburden pressure above shallow tunnels considering the distribution of the principal stress rotation and the partially mobilized arching effect. *Chinese Journal of Rock Mechanics and Engineering* 38 (06), 1284–1296 (In Chinese).
- Wang, Z., Wang, P., Yin, Z., Wang, R., 2022. Micromechanical investigation of the particle size effect on the shear strength of uncrushable granular materials. *Acta Geotech.* 17 (10), 4277–4296. <https://doi.org/10.1007/s11440-022-01501-z>.
- Wang, C., Hou, J., Ye, X.W., Chen, Y.M., Cao, A.W., Huang, L.K., 2023a. In-situ monitoring and 3D numerical analysis of reinforced face behaviour of tunnel in composite strata by considering randomly-distributed rigid cobble granules. *Comput. Geotech.* 156 (4), 105263. <https://doi.org/10.1016/j.compgeo.2023.105263>.
- Wang, P., Yin, Z.Y., Hicher, P.Y., Cui, Y.J., 2023b. Micro-mechanical analysis of one-dimensional compression of clay with DEM. *International Journal for Numerical and Analytical Methods in Geomechanics* 47 (15), 2706–2724.
- Wang, P., Xu, C., Yin, Z.Y., Song, S.X., Xu, C., Dai, S., 2024. A DEM-based Generic Modeling Framework for Hydrate-Bearing Sediments. *Computers and Geotechnics* 171, 106287.
- Wang, T., Wautier, A., Zhu, J., Nicot, F., 2023c. Stabilizing role of coarse grains in cohesionless overfilled binary mixtures: A DEM investigation. *Computers and Geotechnics* 162, 105625. <https://doi.org/10.1016/j.compgeo.2023.105625>.
- Xie, Y., Yang, X., Yang, J., Dai, Y., Liang, X., Gong, F., Zhang, C., 2019. Mesoscopic characteristics of deformation and failure on surrounding rocks of tunnel through loose deposits. *Soils and Rock Mechanics* 40 (12), 4925–4934. (In Chinese).
- Xie, Y., Yang, J., Zheng, X., Qu, T., Zhang, C., Fu, J., 2023. Effect of Particle Size Distributions (PSDs) on ground responses induced by tunneling in dense coarse-grained soils: A DEM investigation. *Comput. Geotech.* 163 (11), 105763. <https://doi.org/10.1016/j.compgeo.2023.105763>.
- Yin, Z., Wang, P., Zhang, F., 2020. Effect of particle shape on the progressive failure of shield tunnel face in granular soils by coupled FDM-DEM method. *Tunn. Undergr. Space Technol.* 100 (6), 103394. <https://doi.org/10.1016/j.tust.2020.103394>.
- Zhao, Y., Gong, Q., Wu, Y., Zornberg, J.G., Tian, Z., Zhang, X., 2021. Evolution of active arching in granular materials: Insights from load, displacement, strain, and particle flow. *Powder Technol.* 384 (5), 160–175. <https://doi.org/10.1016/j.powtec.2021.02.011>.